Computer Methods in Applied Mechanics and Engineering 450 (2026) 118641

Contents lists available at ScienceDirect

Comput. Methods Appl. Mech. Engrg.

journal homepage: www.elsevier.com/locate/cma

A novel finite-strain mixed isogeometric collocation formulation for hyperelastic geometrically exact beams

Diego Ignesti [a], Giulio Ferri [a], Alessandro Reali [b,c], Ferdinando Auricchio [b,c], Josef Kiendl [d], Enzo Marino [a,*]

[a] Department of Civil and Environmental Engineering – University of Florence, Via di S. Marta 3, 50139, Firenze, Italy
[b] Department of Civil Engineering and Architecture, University of Pavia, Via Ferrata, 3, 27100, Pavia, Italy
[c] Istituto di Matematica Applicata e Tecnologie Informatiche "E. Magenes", Consiglio Nazionale delle Ricerche, Pavia, Italy
[d] Institute for Engineering Mechanics and Structural Analysis, University of the Bundeswehr Munich, Werner-Heisenberg-Weg 39, 85579, Neubiberg, Germany

ARTICLE INFO

Keywords:
Geometrically exact beams
Hyperelastic material
Finite strains
Finite rotations
Isogeometric analysis
Isogeometric collocation

ABSTRACT

We propose a novel finite-strain, mixed isogeometric collocation formulation for hyperelastic geometrically exact beams. The model supports general three-dimensional hyperelastic materials and reconstructs the cross-sectional deformation without any modification of the fundamental kinematic assumption typically employed for geometrically exact beams. We express the finite strain components in terms of the one-dimensional geometrically exact strain measures, which allows to exploit existing SO(3)-consistent linearization procedures developed for linearly elastic materials. The governing equations in the strong form are discretized using the isogeometric collocation method (IGA-C). Through various numerical examples, we demonstrate the capability of the model to reproduce both large deformations and finite strains, including the cross-sectional ones, without introducing additional kinematic unknowns.

1. Introduction

Over the last four decades, there has been an unceasing interest in developing theoretical and computational models for the nonlinear mechanics of beam-like elements. Today, in addition to longstanding challenges of traditional engineering fields, new problems are arising in biomechanics, mechanics of metamaterials, soft robotics, programmable objects, additive manufacturing, and beyond. For these problems, continuum-based solid models (see, e.g., [1–4]) turn out to be overly complex and lead to prohibitive computational costs. Advanced beam formulations are an attractive alternative for complex one-dimensional problems, provided they incorporate key features such as the ability to handle finite displacements and rotations, finite strains, nonlinear and rate-dependent materials, and to support arbitrarily curved initial geometries and complex topologies (see, e.g., cardiovascular devices, metamaterials, etc.).

In the framework of linear elasticity, starting from the seminal formulations presented in [5–8], geometrically exact beams have been extensively studied (see, e.g., [9–22]). Models based on the Euler-Bernoulli kinematics have been proposed in [23–28]. Concerning both geometrical and material nonlinearities, Park and Lee [29] were among the first who investigated shear-deformable elastoplastic beams, still keeping the assumption of small strains. Elastoplastic beams have also been addressed in [30–35].

* Corresponding author.
E-mail addresses: diego.ignesti@unifi.it (D. Ignesti), giulio.ferri@unifi.it (G. Ferri), alessandro.reali@unipv.it (A. Reali), ferdinando.auricchio@unipv.it (F. Auricchio), josef.kiendl@unibw.de (J. Kiendl), enzo.marino@unifi.it (E. Marino).

https://doi.org/10.1016/j.cma.2025.118641
Received 24 September 2025; Received in revised form 6 November 2025; Accepted 1 December 2025
Available online 15 December 2025

Geometrically exact, linear viscoelastic beam formulations have been developed in [36–42], for both quasi-static and dynamic problems. Viscoelastic beam structures, featuring arbitrarily curved initial geometry, have been recently addressed in [43,44]. Applications of inelastic nonlinear rod models have been presented in [45].

In most of the mentioned cases, the constitutive models involve only the classical beam resultant forces and associated strains. Such an approach, which has clear advantages in terms of efficiency, may prevent proper characterization of the more realistic three-dimensional behaviour of the beam cross-sections, especially at large strains. Furthermore, another major weakness of existing formulations is that most of them employ nonlinear constitutive relationships neglecting higher order terms in the Green-Lagrange strain tensor, leading to large deformations, small strains formulations [46].

Considering three-dimensional constitutive models for beams, a finite element method (FEM) for finite strain rods has been proposed in [47] incorporating general cross-sectional in-plane distortions and general out-of-plane warping. This is done by introducing additional degrees of freedom. A displacement-based isogeometric finite element formulation for geometrically exact hyperelastic Timoshenko beams has been proposed in [48,49]. This approach, suitable for large strains, permits accounting for cross-section deformations by assuming deformable directors. A hyperelastic model for a modified Timoshenko beam with geometrical and material nonlinearities has been presented in [50]. The nonlinear behaviour and instability of a hyperelastic von Mises truss has been investigated in [51], while hyperelastic Moonley-Rivlin lattice structures have been addressed in [52]. Three-dimensional general constitutive models at moderate and large strains have been considered in [53] and [54], respectively. Here, the beam formulation is enhanced with additional strain variables (i.e., warping functions) for a proper characterization of cross-sectional deformations. In [55] and [56] the constitutive nonlinearity of composite beam structures has been addressed. A polyconvex large strain elasticity formulation for geometrically exact beams has been discussed in [57].

In all the above-mentioned works, three-dimensional nonlinear constitutive models are incorporated in a beam model removing the assumption of rigid cross-section, and thus introducing deformable directors [48,58], and/or using warping functions [30,53]. Although these approaches lead to enhanced formulations, they increase the complexity and number of unknowns of the problem, reducing the overall efficiency.

Klinkel et al. [59] proposed a methodology to use three-dimensional nonlinear constitutive models for the analysis of beams and shells while retaining the respective fundamental kinematic assumptions, i.e., without introducing additional unknowns. They developed a FEM formulation where the three-dimensional material behaviour is retrieved adopting a local plane stress algorithm. Kiendl et al. [60] successfully applied this algorithm to the analysis of hyperelastic Kirchhoff-Love shells.

In the present paper, we propose a novel mixed isogeometric collocation formulation (IGA-C) for the analysis of geometrically exact hyperelastic beams at large strains. The finite strains are expressed as a function of the classical geometrically exact beam deformation measures. Leveraging the method proposed in [59], the three-dimensional hyperelastic constitutive model is adapted to the one-dimensional beam problem such that the cross-section deformation is reconstructed a posteriori without any modification of the original kinematic assumption. The main advantage of this approach is that no additional unknowns are required. In addition to the benefits in terms of computational efficiency, the present formulation allows us to use existing SO(3)-consistent linearizations and updates schemes [43,44,61–63] developed for linearly elastic materials.

Proposed for the first time in [64,65], IGA-C enjoys the same isogeometric analysis (IGA) attributes in terms of geometrical capabilities [66,67]. Moreover, since it discretizes the strong form of the governing equations, it does not require any elements integration [68]. The method requires only one evaluation point (e.g. Greville abscissae) per degree of freedom, entailing high efficiency. IGA-C has been successfully employed for a wide range of beam problems [32,64,65,68–85], including the geometrically exact case [43,44,61–63,86,87]. Additional distinguishing features of the present proposed approach are: the mixed formulation that permits bypassing the linearization of the elastic tangent moduli [32,88] and prevents locking [49,58,62]; the minimum number of rotation unknowns (three, i.e., the incremental rotation vector); the ability to support arbitrarily curved initial geometries [85].

The outline of the paper is as follows. In Section 2, we recall the beam kinematics based on the hypothesis of rigid cross-section. In Section 3, the material models are introduced with a focus on adapting the three-dimensional model to the one-dimensional one. In Section 4, the strong form of the governing equations, their consistent linearization and spatial discretization are presented. Validations of the proposed formulation and numerical examples are presented in Section 5. Finally, the main conclusions are drawn in Section 6.

2. Geometrically exact beam kinematics at finite strains

In this section, we derive the finite strain measures for geometrically exact beams. We start by recalling the kinematics of the Simo-Reissner beam model and by introducing the metric coefficients for the initial and the current configurations of the beam. Then, the relationship between the Green-Lagrange finite strain tensor and the beam deformation measures is presented.

2.1. Beam kinematics and metric tensor

Let $s \mapsto \boldsymbol{c}_0(s) \in \mathbb{R}^3$ be a spatial curve defining the initial position of the beam centroid line. The arc-length $s \in [0, L] \subset \mathbb{R}$, where L denotes the undeformed length of the beam axis.

With $\boldsymbol{\varphi}_0(s, s_2, s_3)$ we denote any point belonging to the undeformed beam cross-section at s (see Fig. 1)

$$\boldsymbol{\varphi}_0(s, s_2, s_3) = \boldsymbol{c}_0(s) + s_2 \boldsymbol{D}_2(s) + s_3 \boldsymbol{D}_3(s) \,. \tag{1}$$

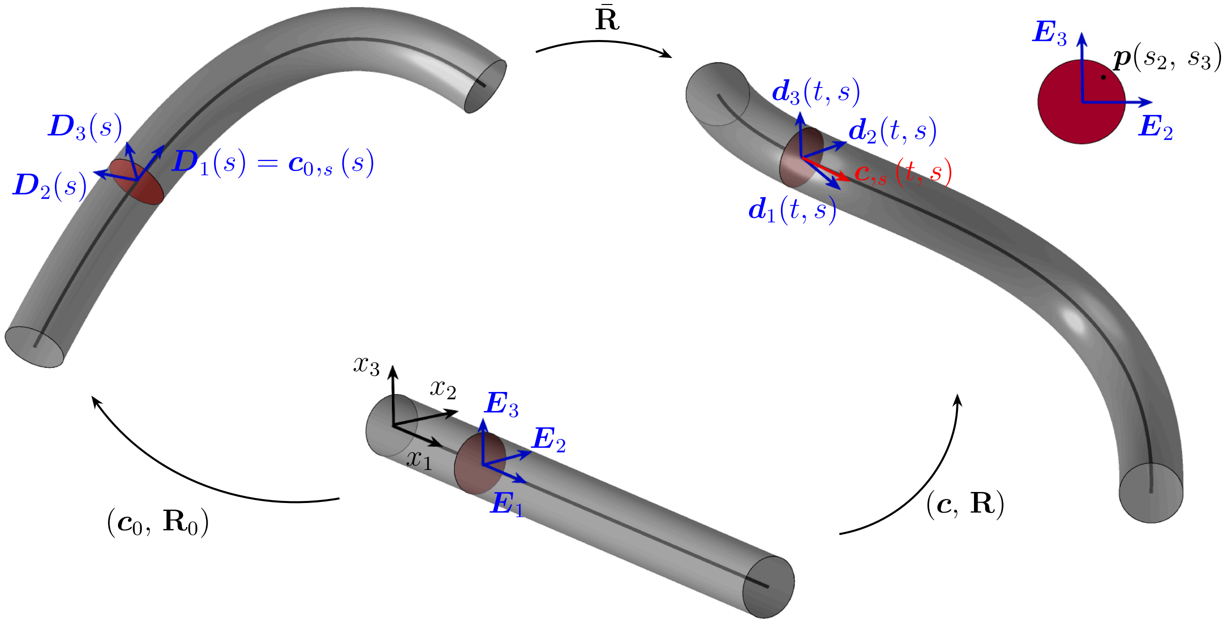

Fig. 1. Beam kinematics in the material (rectilinear), initial and current configurations.

$\{\boldsymbol{D}_1(s), \boldsymbol{D}_2(s), \boldsymbol{D}_3(s)\}$ is an orthonormal local basis whose elements are defined as $\boldsymbol{D}_i(s) = \mathbf{R}_0(s)\boldsymbol{E}_i$, $i = 1,2,3$, with $\boldsymbol{E}_i$ being the ith unit vector of the standard basis of $\mathbb{R}^3$; $\mathbf{R}_0(s) \in SO(3)$[1] is the rotation operator mapping cross-sections from the material (rectilinear) configuration to the initial, curved one; s_2 and s_3 are the coordinates within the cross-section.

It is assumed that, in the initial configuration, cross-sections remain orthogonal to the centroid line $\boldsymbol{c}_0$, leading to $\boldsymbol{D}_1(s) = \boldsymbol{c}_{0,s}(s)$, where $(\cdot)_{,s}$ denotes the derivative with respect to s.

A covariant basis is defined as $\boldsymbol{G}_i = \partial\boldsymbol{\varphi}_0/\partial s_i$, with $i = 1,2,3$ and $s_1 = s$, that is

$$\begin{cases} \boldsymbol{G}_1(s,s_2,s_3) = \boldsymbol{D}_1(s) + s_2\boldsymbol{D}_{2,s}(s) + s_3\boldsymbol{D}_{3,s}(s) \\ \boldsymbol{G}_\alpha(s,s_2,s_3) = \boldsymbol{D}_\alpha(s)\,. \end{cases} \tag{2}$$

Note that in the above equations $\boldsymbol{D}_{\alpha,s}(s) = \widetilde{\boldsymbol{k}}_0(s)\boldsymbol{D}_\alpha(s)$, $\alpha = 2,3$, where $\widetilde{\boldsymbol{k}}_0(s) := \mathbf{R}_{0,s}(s)\mathbf{R}_0^{\mathrm{T}}(s)$[2] is the initial (skew-symmetric) curvature tensor in spatial form.

The contravariant basis, $\boldsymbol{G}^i$, defined such that $\boldsymbol{G}^j \cdot \boldsymbol{G}_i = \delta_i^j$, where δ_i^j is the Kronecker delta, is given by $\boldsymbol{G}^i = G^{ij}\boldsymbol{G}_j$ where $G^{ij} = G_{ij}^{-1}$ and $G_{ij} = \boldsymbol{G}_i \cdot \boldsymbol{G}_j$. In an explicit form, the contravariant basis co-vectors are given as follows

$$\begin{cases} \boldsymbol{G}^1(s,s_2,s_3) = \dfrac{1}{C}\boldsymbol{D}_1(s), \\ \boldsymbol{G}^2(s,s_2,s_3) = \dfrac{s_3K_{01}}{C}\boldsymbol{D}_1(s) + \boldsymbol{D}_2(s), \\ \boldsymbol{G}^3(s,s_2,s_3) = \dfrac{-s_2K_{01}}{C}\boldsymbol{D}_1(s) + \boldsymbol{D}_3(s), \end{cases} \tag{3}$$

where $C = 1 - s_2K_{03} + s_3K_{02}$, and K_{0_α} are the components of the initial curvature vector $\boldsymbol{K}_0(s) = \mathrm{axial}(\widetilde{\boldsymbol{K}}_0(s))$, associated with $\widetilde{\boldsymbol{K}}_0(s) := \mathbf{R}_0^{\mathrm{T}}(s)\mathbf{R}_{0,s}(s)$. Note that both $\boldsymbol{K}_0$ and $\widetilde{\boldsymbol{K}}_0$ are here expressed in the material form.

The current (deformed) configuration of the beam centroid line is represented by the spatial curve $s \mapsto \boldsymbol{c}(t,s) \in \mathbb{R}^3$, where $t \in [0,T] \subset \mathbb{R}^+$ where T is the time domain. Similarly to what has been done for the initial configuration, $\boldsymbol{\varphi}(t,s,s_2,s_3)$ defines the current position of any point belonging to the beam cross-section at s and at time t (see Fig. 1) as

$$\boldsymbol{\varphi}(t,s,s_2,s_3) = \boldsymbol{c}(t,s) + s_2\boldsymbol{d}_2(t,s) + s_3\boldsymbol{d}_3(t,s)\,. \tag{4}$$

$\{\boldsymbol{d}_1(t,s), \boldsymbol{d}_2(t,s), \boldsymbol{d}_3(t,s)\}$ is the local basis of the current configuration defined as $\boldsymbol{d}_i(t,s) = \mathbf{R}(t,s)\boldsymbol{E}_i$, being $\mathbf{R}(t,s)$ the rotation operator mapping the cross-sections from the material (rectilinear) configuration to the current one. Also in this case, we define a covariant

[1] SO(3) denotes the Special Orthogonal group. Namely, it is the (Lie) group of rotations in $\mathbb{R}^3$. An element $\mathbf{R} \in SO(3)$ is such that $\mathbf{R}^{\mathrm{T}} = \mathbf{R}^{-1}$ and $\det(\mathbf{R}) = 1$.

[2] With the symbol $\sim$ we mark elements of $so(3)$, that is the set of 3×3 skew-symmetric matrices. In this context, they are used to represent curvature matrices and infinitesimal incremental rotations. Furthermore, we recall that for any skew-symmetric matrix $\widetilde{\boldsymbol{a}} \in so(3)$, $\boldsymbol{a} = \mathrm{axial}(\widetilde{\boldsymbol{a}})$ indicates the axial vector of $\widetilde{\boldsymbol{a}}$ such that $\widetilde{\boldsymbol{a}}\boldsymbol{h} = \boldsymbol{a} \times \boldsymbol{h}$, for any $\boldsymbol{h} \in \mathbb{R}^3$, where $\times$ is the cross product.

basis $\boldsymbol{g}_i = \partial\boldsymbol{\varphi}/\partial s_i$ given by

$$\begin{cases} \boldsymbol{g}_1(t,s,s_2,s_3) = \boldsymbol{c},_s(t,s) + s_2\boldsymbol{d}_{2,s}(t,s) + s_3\boldsymbol{d}_{3,s}(t,s) \\ \boldsymbol{g}_\alpha(t,s,s_2,s_3) = \boldsymbol{d}_2(t,s), \end{cases} \tag{5}$$

with $\boldsymbol{d}_{\alpha,s}(t,s) = \widetilde{\boldsymbol{k}}(t,s)\boldsymbol{d}_\alpha(t,s)$, $\alpha = 2,3$. $\widetilde{\boldsymbol{k}}(t,s) := \mathbf{R},_s(t,s)\mathbf{R}^{\mathsf{T}}(t,s)$ is the current curvature tensor in spatial form. Note that, due to the shear deformation, the beam cross-sections may not remain orthogonal to the centroid line at time t. Therefore, the tangent vector to the beam centroid, $\boldsymbol{c},_s(t,s)$, and the normal vector to the beam cross-section, $\boldsymbol{d}_1(t,s)$, in general do not coincide. Note that, from now on, we omit the variable t, which remains implicit in all quantities referred to the current configuration.

2.2. Deformation gradient in terms of beam strain measures

For a general continuum, the deformation gradient tensor, $\mathbf{F}$, can be expressed as

$$\mathbf{F} = \boldsymbol{g}_i \otimes \boldsymbol{G}^i\,. \tag{6}$$

To express $\mathbf{F}$ through the basis vectors of the initial, $\boldsymbol{D}_i$, and current, $\boldsymbol{d}_i$, configurations of the beam, it is convenient to first recall the beam deformation measures in the material setting defined as follows [61]

$$\boldsymbol{\Gamma}_N = \mathbf{R}^{\mathsf{T}}\boldsymbol{c},_s - \mathbf{R}_0^{\mathsf{T}}\boldsymbol{c}_{0,s}, \tag{7}$$

$$\boldsymbol{K}_M = \mathrm{axial}(\widetilde{\boldsymbol{K}} - \widetilde{\boldsymbol{K}}_0), \tag{8}$$

where $\widetilde{\boldsymbol{K}} = \mathbf{R}^{\mathsf{T}}\mathbf{R},_s$ is the current curvature tensor in the material form.

By substituting Eqs. (3) and (5) into (6), we can rewrite $\mathbf{F}$ using the polar decomposition

$$\mathbf{F} = \bar{\mathbf{R}}\mathbf{U}, \tag{9}$$

where $\bar{\mathbf{R}} = \mathbf{R}\mathbf{R}_0{}^{\mathsf{T}} = \boldsymbol{d}_i \otimes \boldsymbol{D}_i$ is the relative rotation operator mapping the orientation of cross-sections from the initial to the current configuration (see Fig. 1) and $\mathbf{U}$ is the pure strain tensor at the initial configuration

$$\mathbf{U} = \mathbf{I} + \frac{1}{C}\boldsymbol{H} \otimes \boldsymbol{D}_1, \tag{10}$$

where $\mathbf{I}$ is the identity matrix in $\mathbb{R}^{3\times3}$, while $\boldsymbol{H}$ is the material strain vector defined as [57]

$$\boldsymbol{H} = \mathbf{R}_0\left(\boldsymbol{\Gamma}_N + \widetilde{\boldsymbol{K}}_M(s_2\boldsymbol{E}_2 + s_3\boldsymbol{E}_3)\right). \tag{11}$$

We remark that this definition of the material strain vector permits accounting for both straight and arbitrarily curved initial geometries with no restrictions.

Finally, the deformation gradient in terms of the beam deformation measures is obtained as follows

$$\mathbf{F} = \bar{\mathbf{R}}\left[\mathbf{I} + \frac{1}{C}\mathbf{R}_0\left(\boldsymbol{\Gamma}_N + \widetilde{\boldsymbol{K}}_M(s_2\boldsymbol{E}_2 + s_3\boldsymbol{E}_3)\right) \otimes \boldsymbol{D}_1\right]. \tag{12}$$

Note that the expression of $\mathbf{F}$ as a function of the beam strain measures plays a pivotal role in our formulation since it will allow to use the standard SO(3)-consistent linearization formulae normally used for linear elastic materials at small strains.

2.2.1. Green-Lagrange strain tensor

We start from the definition of the Green-Lagrange strain tensor $\mathbf{E} = \mathrm{E}_{ij}(\boldsymbol{G}^i \otimes \boldsymbol{G}^j) = \frac{1}{2}(\mathbf{F}^{\mathsf{T}}\mathbf{F} - \mathbf{I})$, which, making use of Eq. (12), becomes [40]

$$\mathbf{E} = \frac{1}{2C}(\boldsymbol{H} \otimes \boldsymbol{D}_1 + \boldsymbol{D}_1 \otimes \boldsymbol{H}) + \frac{\boldsymbol{H}^2}{2C^2}(\boldsymbol{D}_1 \otimes \boldsymbol{D}_1) = \mathrm{E}_{ij}(\boldsymbol{D}_i \otimes \boldsymbol{D}_j)\,. \tag{13}$$

Eq. (13) can be simplified enforcing the small strain assumption, i.e., neglecting the second term, and setting $C = 1$. This hypothesis is often used in the literature, also for geometrically exact beams [61,62,65]. However, this simplification may lead to erroneous predictions of the beam response, especially when material nonlinearities are taken into account.

To develop a finite strain beam formulation, where both geometry and material nonlinearities are considered, we express explicitly the local Cartesian components of the Green-Lagrange strain tensor $\mathrm{E}_{ij} = \boldsymbol{D}_i^{\mathsf{T}}\mathbf{E}\boldsymbol{D}_j$ as a function of $\boldsymbol{\Gamma}_N$ and $\boldsymbol{K}_M$

$$\begin{aligned}
\mathrm{E}_{11} = {} & \frac{1}{C}[\Gamma_{N_1} + K_{M_2}s_3 - K_{M_3}s_2] + \frac{1}{2C^2}\boldsymbol{\Gamma}_N^{\mathsf{T}}\boldsymbol{\Gamma}_N + \frac{1}{C^2}\Gamma_{N_1}(K_{M_2}s_3 - K_{M_3}s_2) \\
& - \frac{1}{C^2}\Gamma_{N_2}(K_{M_1}s_3) + \frac{1}{C^2}\Gamma_{N_3}(K_{M_1}s_2) + \frac{1}{2C^2}K_{M_1}^2({s_2}^2 + {s_3}^2) + \frac{1}{2C^2}K_{M_2}^2{s_3}^2 \\
& + \frac{1}{2C^2}K_{M_3}^2{s_2}^2 - \frac{1}{C^2}K_{M_2}K_{M_3}s_2s_3,
\end{aligned} \tag{14}$$

$$\mathrm{E}_{12} = \mathrm{E}_{21} = \frac{1}{2C}[\Gamma_{N_2} - K_{M_1}s_3],$$

$$\mathrm{E}_{13} = \mathrm{E}_{31} = \frac{1}{2C}[\Gamma_{N_3} + K_{M_1}s_2]\,.$$

where Γ_{N_i} and K_{M_i} are the ith components of the beam strain measures with respect to the base vector $\boldsymbol{E}_i$. Note that the remaining components $\mathrm{E}_{22} = \mathrm{E}_{33} = \mathrm{E}_{23} = \mathrm{E}_{32} = 0$ vanish according to the kinematic assumption.

3. Constitutive equations

To account for cross-sectional deformations, we use the local plane stress algorithm proposed in [59], which requires a modification of the material elastic tensor. For the sake of completeness, we start by recalling the constitutive relationship for hyperelastic materials at finite strains.

3.1. The local plane stress algorithm for hyperelastic beams

Consider a general hyperelastic material with a strain energy function $\psi(\mathbf{E})$. The stress-strain relationship reads as follows

$$\mathbf{S} = \frac{\partial \psi(\mathbf{E})}{\partial \mathbf{E}}, \tag{15}$$

where $\mathbf{S} = \mathrm{S}^{ij}(\boldsymbol{G}_i \otimes \boldsymbol{G}_j)$ is the second Piola-Kirchhoff stress tensor whose components are $\mathrm{S}^{ij} = \partial\psi/\partial \mathrm{E}_{ij}$.

In general, the second Piola-Kirchhoff stress tensor $\mathbf{S}$ is a nonlinear tensor-valued function of the Green-Lagrange strain tensor $\mathbf{E}$; therefore, in the linearization process, it is required to compute the tangent material tensor $\mathbb{C} = \mathrm{C}^{ijkl}(\boldsymbol{G}_i \otimes \boldsymbol{G}_j \otimes \boldsymbol{G}_k \otimes \boldsymbol{G}_l)$ given by

$$\mathbb{C} = \frac{\partial \mathbf{S}}{\partial \mathbf{E}}. \tag{16}$$

In the classical beam theory, the equilibrium in the plane of the beam cross-section leads to a stress tensor such that S^{22}, S^{33} and S^{23} vanish [30,59]. We now enforce this condition in order to compute *a posteriori* the resulting strains which would instead be zero according to the beam kinematic assumption (Eq. (4)). To do so, the tangent material tensor must be redefined accordingly. We first rewrite stress and strain components in Voigt notation as

$$\mathbf{S} = [\mathrm{S}^{11}, \mathrm{S}^{12}, \mathrm{S}^{13}, \mathrm{S}^{22}, \mathrm{S}^{33}, \mathrm{S}^{23}]^{\mathsf{T}}, \quad \mathbf{E} = [\mathrm{E}_{11}, \mathrm{E}_{12}, \mathrm{E}_{13}, \mathrm{E}_{22}, \mathrm{E}_{33}, \mathrm{E}_{23}]^{\mathsf{T}}, \tag{17}$$

and we introduce $\mathbf{S}_m = [\mathrm{S}^{11}, \mathrm{S}^{12}, \mathrm{S}^{13}]^{\mathsf{T}}$, $\mathbf{S}_z = [\mathrm{S}^{22}, \mathrm{S}^{33}, \mathrm{S}^{23}]^{\mathsf{T}}$, $\mathbf{E}_m = [\mathrm{E}_{11}, \mathrm{E}_{12}, \mathrm{E}_{13}]^{\mathsf{T}}$ and $\mathbf{E}_z = [\mathrm{E}_{22}, \mathrm{E}_{33}, \mathrm{E}_{23}]^{\mathsf{T}}$. We make use of the algorithm proposed in [59] to enforce the condition $\mathbf{S}_z = \mathbf{0}$ and to reconstruct the strain components $\mathbf{E}_z$. Note that this is done computing an updated (3×3) material tangent tensor, $\mathbb{C}_{up}$, relating $\mathbf{S}_m$ with $\mathbf{E}_m$. For a detailed description of this method, we refer to [59] and Appendix A.

3.2. Stress resultants and stress couples

The resultant of the internal forces $\boldsymbol{n}$ in the current configuration is defined by

$$\boldsymbol{n} := \int_{A_0} \mathbf{P}\boldsymbol{D}_1 \, dA_0, \tag{18}$$

where $\mathbf{P} = \mathrm{P}^{ij}(\boldsymbol{g}_i \otimes \boldsymbol{G}_j)$ is the first Piola-Kirchhoff stress tensor. We remark that, due to the two-point nature of $\mathbf{P}$, the integration is performed over the beam undeformed area, A_0, whose normal vector is $\boldsymbol{D}_1 = C\boldsymbol{G}^1$.

Similarly, the resultant of the internal couples $\boldsymbol{m}$ in the current configuration reads as follows

$$\boldsymbol{m} = \int_{A_0} (s_2 \boldsymbol{d}_2 + s_3 \boldsymbol{d}_3) \times \mathbf{P}\boldsymbol{D}_1 \, dA_0 \,. \tag{19}$$

Introducing the second Piola-Kirchhoff stress tensor, $\mathbf{S} = \mathrm{S}^{ij}(\boldsymbol{G}_i \otimes \boldsymbol{G}_j)$, and recalling that $\mathbf{P} = \mathbf{F}\mathbf{S}$, Eqs. (18) and (19) become

$$\boldsymbol{n} = \int_{A_0} \mathbf{F}\mathbf{S}C\boldsymbol{G}^1 \, dA_0, \tag{20}$$

$$\boldsymbol{m} = \int_{A_0} (s_2 \boldsymbol{d}_2 + s_3 \boldsymbol{d}_3) \times \mathbf{F}\mathbf{S}C\boldsymbol{G}^1 \, dA_0 \,. \tag{21}$$

Considering that $\boldsymbol{d}_i = \bar{\mathbf{R}}\boldsymbol{D}_i$ and making use of the polar decomposition of $\mathbf{F}$ given in Eq. (12), we are now able to express the beam internal forces and couples in terms of the beam deformation measures, $\boldsymbol{\Gamma}_N$ and $\boldsymbol{K}_M$, as follows

$$\boldsymbol{n} = \bar{\mathbf{R}} \int_{A_0} \left[\mathbf{I} + \frac{1}{C} \mathbf{R}_0 \left(\boldsymbol{\Gamma}_N + \boldsymbol{K}_\xi \right) \otimes \boldsymbol{D}_1 \right] \mathbf{S}C\boldsymbol{G}^1 \, dA_0, \tag{22}$$

$$\boldsymbol{m} = \bar{\mathbf{R}} \int_{A_0} (\widetilde{s_2 \boldsymbol{D}_2 + s_3 \boldsymbol{D}_3}) \left[\left(\mathbf{I} + \frac{1}{C} \mathbf{R}_0 \left(\boldsymbol{\Gamma}_N + \boldsymbol{K}_\xi \right) \otimes \boldsymbol{D}_1 \right) \mathbf{S}C\boldsymbol{G}^1 \right] dA_0, \tag{23}$$

where we have set $\boldsymbol{K}_\xi = \widetilde{\boldsymbol{K}}_M (s_2 \boldsymbol{E}_2 + s_3 \boldsymbol{E}_3)$.

4. Governing equations

For geometrically exact beams, the strong form version of the governing equations reads as

$$\boldsymbol{n}_{,s} + \bar{\boldsymbol{n}} = \boldsymbol{0}, \tag{24}$$

$$\boldsymbol{m}_{,s} + \boldsymbol{c}_{,s} \times \boldsymbol{n} + \bar{\boldsymbol{m}} = \boldsymbol{0}, \tag{25}$$

where $\bar{\boldsymbol{n}}$ and $\bar{\boldsymbol{m}}$ are the spatial distributed external forces and moments per unit-length. The above balance equations need to be completed by Neumann and/or Dirichlet Boundary Conditions (BCs) at the beam ends [62]. Moreover, in the mixed formulation we propose, in addition to Eqs. (24) and (25) (with appropriate BCs), the system we solve includes Eqs. (22) and (23), for a total of four equations. The four variables are the incremental fields: spatial displacements, $\delta\boldsymbol{\eta}$; spatial rotations, $\delta\boldsymbol{\vartheta}$; spatial forces, $\delta\boldsymbol{n}$; spatial couples, $\delta\boldsymbol{m}$.

4.1. SO(3)–Consistent linearization of the governing equation and their discretization

To define the tangent matrix needed in the Newton-Raphson algorithm, the governing equations need to be linearized letting the incremental variables appear explicitly. To do so, we first reformulate Eqs. (22) and (23) to let the components of the second Piola-Kirchhoff stress tensor appear as follows

$$\begin{aligned}\boldsymbol{n} = \bar{\mathbf{R}} \int_{A_0} & \mathrm{S}^{11} C(\mathbf{R}_0 \boldsymbol{\Gamma}_N) + \mathrm{S}^{11} C \mathbf{R}_0 \boldsymbol{K}_\xi + \mathrm{S}^{11} C^2 \boldsymbol{D}_1 - s_3 K_{01} \mathrm{S}^{11} C \boldsymbol{D}_2 \\ & + s_2 K_{01} \mathrm{S}^{11} C \boldsymbol{D}_3 + \mathrm{S}^{21} C \boldsymbol{D}_2 + \mathrm{S}^{31} C \boldsymbol{D}_3 \, dA_0,\end{aligned} \tag{26}$$

$$\begin{aligned}\boldsymbol{m} = \bar{\mathbf{R}} \int_{A_0} & (\widetilde{s_2 \boldsymbol{D}_2 + s_3 \boldsymbol{D}_3}) \Big[\mathrm{S}^{11} C(\mathbf{R}_0 \boldsymbol{\Gamma}_N) + \mathrm{S}^{11} C \mathbf{R}_0 \boldsymbol{K}_\xi + \mathrm{S}^{11} C^2 \boldsymbol{D}_1 \\ & - s_3 K_{01} \mathrm{S}^{11} C \boldsymbol{D}_2 + s_2 K_{01} \mathrm{S}^{11} C \boldsymbol{D}_3 + \mathrm{S}^{21} C \boldsymbol{D}_2 + \mathrm{S}^{31} C \boldsymbol{D}_3 \Big] dA_0 .\end{aligned} \tag{27}$$

Since S^{i1}, i = 1, 2, 3, are functions of the Green-Lagrange strain tensor $\mathbf{E}$ through the strain energy function $\psi(\mathbf{E})$, all the quantities appearing in the left hand side of Eqs. (26) and (27) are expressed in terms of kinematic quantities. In this way, the whole set of equations (Eqs. (24), (25), (26) and (27)) has now been conveniently reformulated in order to use existing SO(3)-consistent linearizations [61].

The linearized form of Eqs. (24), (25) and Eqs. (26), (27) is given as

$$\delta\boldsymbol{n}_{,s} = -(\hat{\boldsymbol{n}}_{,s} + \bar{\boldsymbol{n}}), \tag{28}$$

$$\delta\boldsymbol{m}_{,s} - \hat{\tilde{\boldsymbol{n}}} \delta\boldsymbol{\eta}_{,s} + \hat{\tilde{\boldsymbol{c}}}_{,s} \delta\boldsymbol{n} = -(\hat{\boldsymbol{m}}_{,s} + \hat{\tilde{\boldsymbol{c}}}_{,s} \hat{\boldsymbol{n}} + \bar{\boldsymbol{m}}), \tag{29}$$

$$\delta\boldsymbol{n} - \hat{\bar{\mathbf{R}}} \hat{\boldsymbol{T}}_{\eta\eta} \delta\boldsymbol{\eta}_{,s} + \left[\widetilde{\left(\hat{\bar{\mathbf{R}}} \hat{\boldsymbol{T}}^1_{\eta\vartheta} \right)} - \hat{\bar{\mathbf{R}}} \hat{\boldsymbol{T}}^2_{\eta\vartheta} \right] \delta\boldsymbol{\vartheta} - \hat{\bar{\mathbf{R}}} \hat{\boldsymbol{T}}^3_{\eta\vartheta} \delta\boldsymbol{\vartheta}_{,s} = -\hat{\boldsymbol{n}} + \hat{\bar{\mathbf{R}}} \hat{\boldsymbol{T}}_n, \tag{30}$$

$$\delta\boldsymbol{m} - \hat{\bar{\mathbf{R}}} \hat{\boldsymbol{T}}_{\vartheta\eta} \delta\boldsymbol{\eta}_{,s} + \left[\widetilde{\left(\hat{\bar{\mathbf{R}}} \hat{\boldsymbol{T}}^1_{\vartheta\vartheta} \right)} - \hat{\bar{\mathbf{R}}} \hat{\boldsymbol{T}}^2_{\vartheta\vartheta} \right] \delta\boldsymbol{\vartheta} - \hat{\bar{\mathbf{R}}} \hat{\boldsymbol{T}}^3_{\vartheta\vartheta} \delta\boldsymbol{\vartheta}_{,s} = -\hat{\boldsymbol{n}} + \hat{\bar{\mathbf{R}}} \hat{\boldsymbol{T}}_m . \tag{31}$$

where $\hat{\boldsymbol{T}}_{\eta\eta}$ and $\hat{\boldsymbol{T}}_{\vartheta\eta}$ are the integral quantities appearing respectively in the internal force and couples equations, that are associated with the translational unknowns; $\hat{\boldsymbol{T}}^i_{\eta\vartheta}$, $i = 1, 2, 3$, are integral quantities related to the rotational unknowns; similarly, $\hat{\boldsymbol{T}}^i_{\vartheta\vartheta}$, $i = 1, 2, 3$, are the integrals associated with the rotational unknowns. Lastly, with $\hat{\boldsymbol{T}}_n$ and $\hat{\boldsymbol{T}}_m$ we denote integral quantities that are directly contributing to the current internal forces and couples, $\hat{\boldsymbol{n}}$ and $\hat{\boldsymbol{m}}$, respectively.

We remark that Eqs. (28) and (29) hold for $s \in (0, L)$, whereas (30), (31) are valid for $s \in [0, L]$. For a more detailed description of the linearization procedure, the reader is referred to Appendix B, where we also provide the expression of the above integral quantities. For the linearization of the Dirichlet and/or Neumann BCs at $s \in \{0, L\}$ we refer to [62].

4.2. IGA Discretization and collocation of the linearized equations

The linearized governing equations are discretized in space using NURBS basis functions and collocated at the Greville abscissae [64]. The kinematic variables of the problem are discretized as

$$\boldsymbol{c}(u) = \sum_{j=1}^{\mathrm{n}} R_{j,p}(u) \check{\boldsymbol{p}}_j \quad \text{with} \quad u \in [0, 1], \tag{32}$$

$$\delta\boldsymbol{\vartheta}(u) = \sum_{j=1}^{\mathrm{n}} R_{j,p}(u) \delta\check{\boldsymbol{\vartheta}}_j \quad \text{with} \quad u \in [0, 1], \tag{33}$$

$$\delta\boldsymbol{\eta}(u) = \sum_{j=1}^{\mathrm{n}} R_{j,p}(u) \delta\check{\boldsymbol{\eta}}_j \quad \text{with} \quad u \in [0, 1], \tag{34}$$

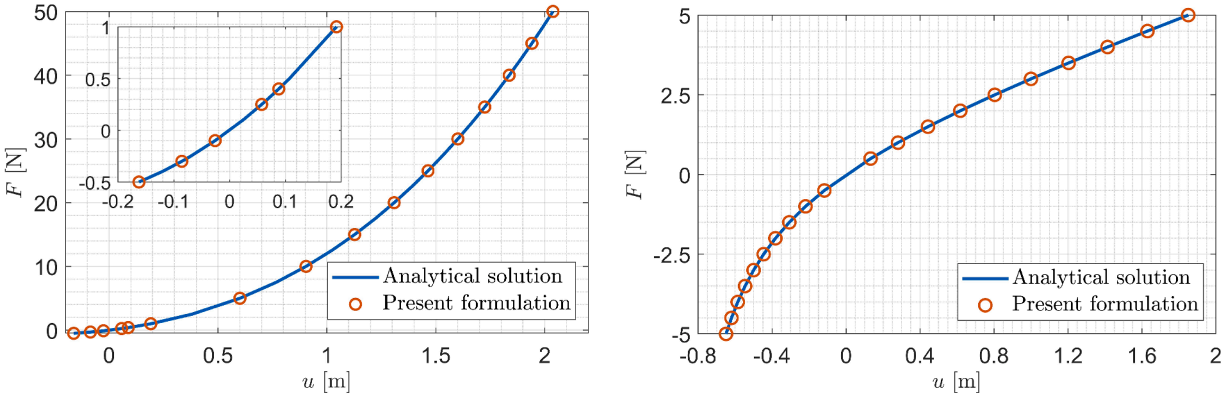

(a) SVK material.

(b) Compressible NH material.

Fig. 2. Uniaxial tension of a cantilever straight beam: applied load, F_1, vs. axial displacement, u_1.

Table 1
Exact initial geometry of the circular arch with $p = 2$ NURBS basis functions and 3 control points.

	x_1 [m]	x_2 [m]	x_3 [m]	w [−]
$\check{p}_1$	0	0	0	1
$\check{p}_2$	$R\tan(3/8\pi)$	0	$R\tan(3/32\pi)$	$\cos(3/8\pi)$
$\check{p}_3$	$R\sin(3/4\pi)$	$R(1-\cos(3/4\pi))$	$R\tan(3/16\pi)$	1

where $R_{j,p}$ ($j = 1,\dots,\mathrm{n}$) is the jth NURBS of degree p; $\check{\boldsymbol{p}}_j$ are the coordinates of the jth control point of the beam axis, while $\delta\check{\boldsymbol{\vartheta}}_j$ and $\delta\check{\boldsymbol{\eta}}_j$ are the jth control variables of the incremental spatial rotation and translation, respectively. In the same way, the spatial incremental forces, $\delta\boldsymbol{n}$, and couples, $\delta\boldsymbol{m}$, are discretized in space as

$$\delta\boldsymbol{n}(u) = \sum_{j=1}^{\mathrm{n}} R_{j,p}(u)\delta\check{\boldsymbol{n}}_j \quad \text{with} \quad u \in [0,\ 1], \tag{35}$$

$$\delta\boldsymbol{m}(u) = \sum_{j=1}^{\mathrm{n}} R_{j,p}(u)\delta\check{\boldsymbol{m}}_j \quad \text{with} \quad u \in [0,\ 1], \tag{36}$$

where $\delta\check{\boldsymbol{n}}_j$ and $\delta\check{\boldsymbol{m}}_j$ are the jth control variables of $\delta\boldsymbol{n}(u)$ and $\delta\boldsymbol{m}(u)$, respectively. Inside the Newton-Raphson iterative scheme, once the primal variables are calculated, we adopt the same SO(3)-consistent geometry updating procedure proposed in [62]. Once the system is solved and the control incremental rotations, $\delta\check{\boldsymbol{\vartheta}}_j^k$, are computed, the incremental spatial rotation vector is evaluated at the ith collocation point, u_i^c, as follows

$$\delta\boldsymbol{\vartheta}^k(u_i^c) = \sum_{j=1}^{\mathrm{n}} R_{j,p}(u_i^c)\delta\check{\boldsymbol{\vartheta}}_j^k \quad \text{with} \quad i, j = 1,\dots,\mathrm{n}\,.$$

With this value, the rotation operator is consistently updated (at the collocation point) using the exponential map of SO(3) as

$$\hat{\mathbf{R}}^{k+1}(u_i^c) = \exp(\delta\widetilde{\boldsymbol{\vartheta}}^k(u_i^c))\hat{\mathbf{R}}^k(u_i^c) \quad \text{for} \quad i = 1,\dots,\mathrm{n}\,. \tag{37}$$

Similarly, the curvature tensor at the ith collocation point is updated by exploiting the derivative of the exponential map as

$$\hat{\tilde{\boldsymbol{K}}}^{k+1}(u_i^c) = \hat{\tilde{\boldsymbol{K}}}^k(u_i^c) + \hat{\mathbf{R}}^{k\mathrm{T}}(u_i^c) d\exp_{\delta\widetilde{\boldsymbol{\vartheta}}^k}(\delta\widetilde{\boldsymbol{\vartheta}}^k(u_i^c)_{,s})\hat{\mathbf{R}}(u_i^c)^k \quad \text{for} \quad i = 1,\dots,\mathrm{n}\,. \tag{38}$$

For the expression of the exponential map of SO(3) and the approximation of its derivative, we can refer to [61].

5. Numerical examples

In this section, we report a series of numerical examples aimed at testing all the attributes of the proposed model. We start with two benchmark tests of uniaxial tension, where the numerical results are compared with analytical solutions at large strains. Then, a circular arch under out-of-plane load is considered. For this test, we also assess that the higher-order spatial accuracy, typical of IGA-C, is preserved. Finally, two examples of beams with complex three-dimensional initial curvature under large deformations and strains are presented.

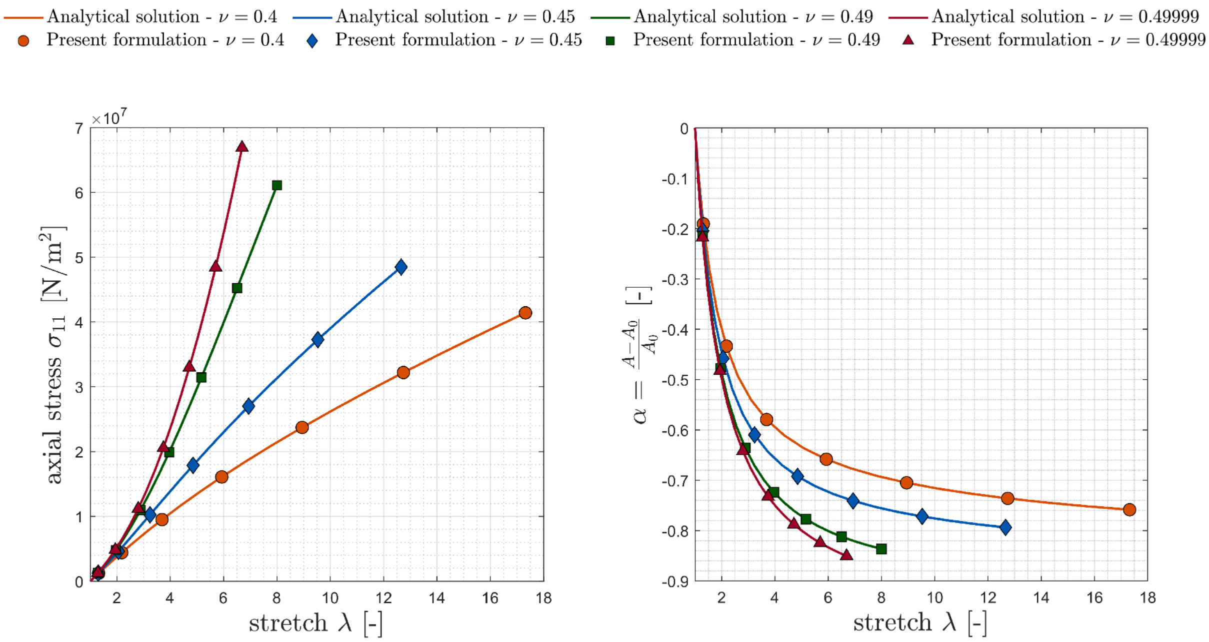

(a) Cauchy stress component, σ_{11}, vs. stretch, λ.

(b) Area dilatation, α, vs. stretch, λ.

Fig. 3. Traction test for the Neo-Hookean material with different Poisson's ratio.

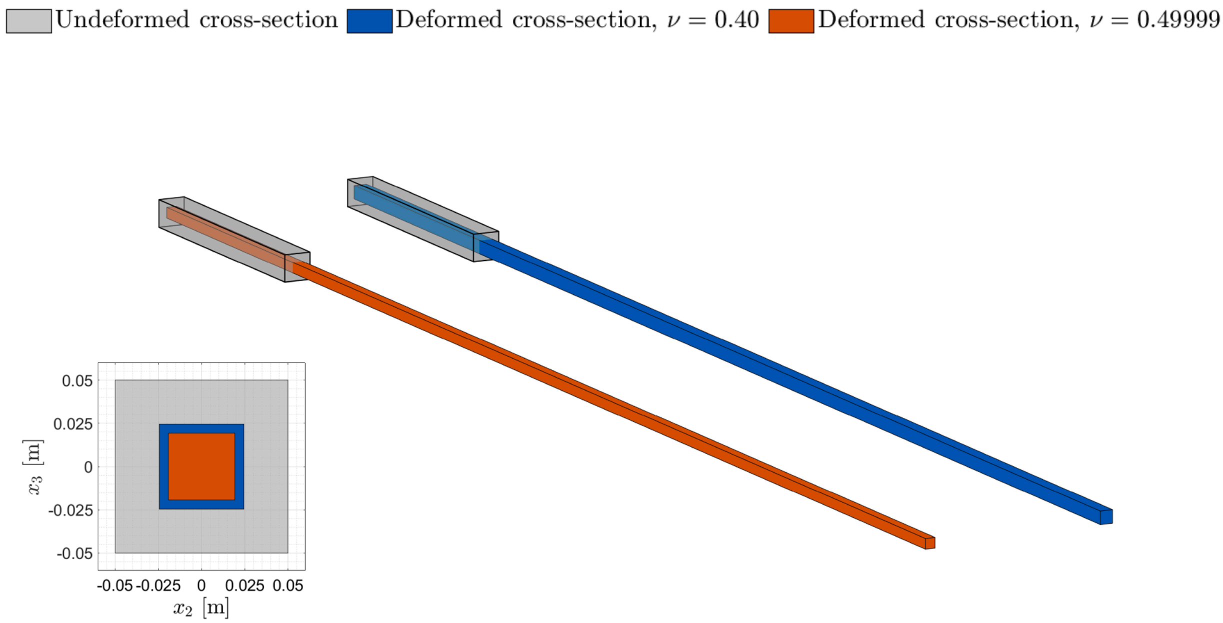

Fig. 4. Traction test for the Neo-Hookean material with two different Poisson's ratio, $\nu = 0.4$ and $\nu = 0.49999$: comparisons in terms of the cross-section deformations for the same value of the stretch, $\lambda = 6$.

5.1. Uniaxial tension of a straight beam at finite strains

In this numerical example, we assess the capability of the present method to account for finite strains. Hyperelastic materials whose strain energy functions are characterized by Young Modulus, $E = 100\,\mathrm{N/m^2}$, and Poisson ratio, $\nu = 0$, are considered. In this case, no cross-sectional deformations occur. Therefore, the local plane stress algorithm will return $\mathbf{E}_z = 0$. Still, the beam will undergo finite strains, leading to nonlinear solutions that are compared with the analytical ones derived from [89].

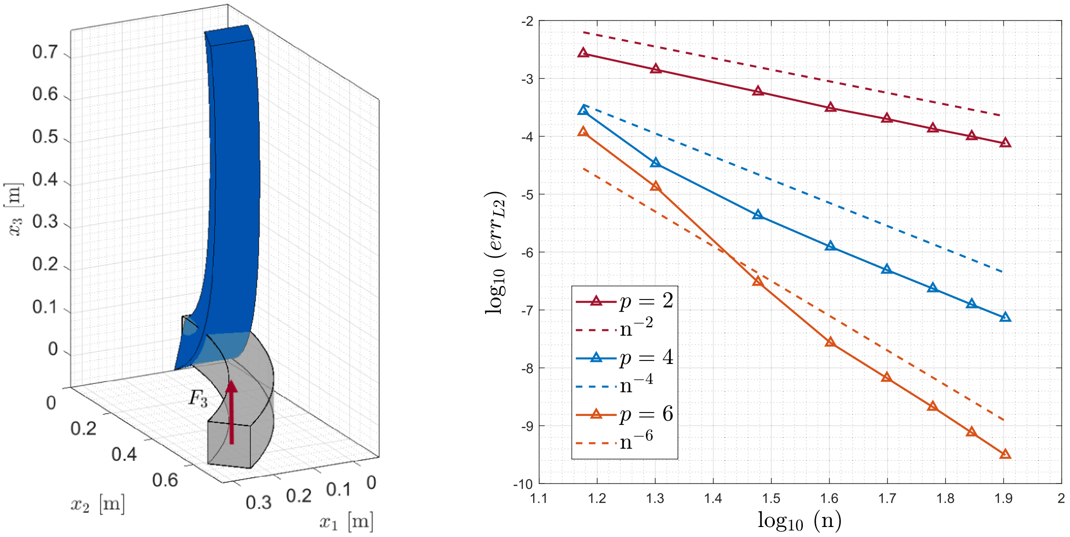

(a) Extrude view. (b) Convergence plots.

Fig. 5. Deformed shape of the 45° circular arch: extrude view and individuation of the load applied (a). Convergence plots for $p = 2, 4, 6$ of the L_2 norm of error vs. number of collocation points (b).

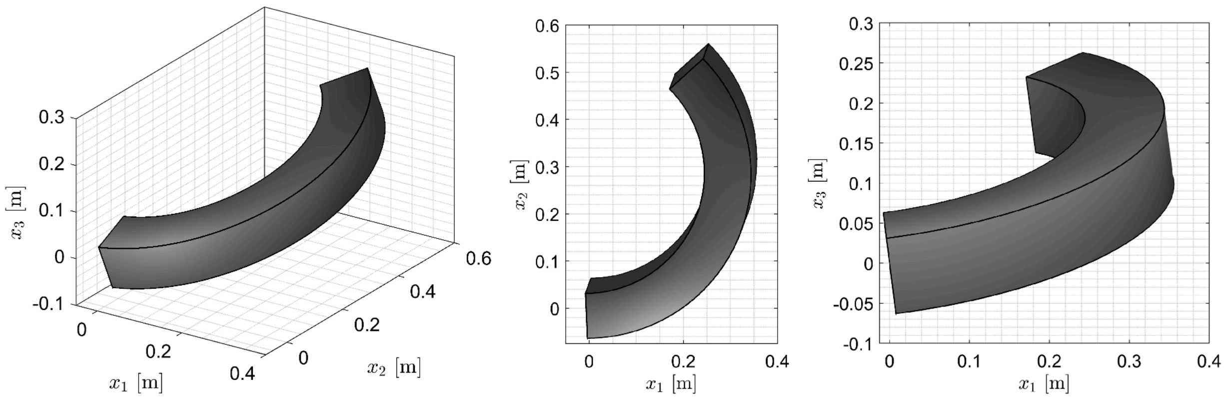

(a) 3D view. (b) Planar (x_1, x_2) view. (c) Planar (x_1, x_3) view.

Fig. 6. Straightening of a circular arch: initial configuration.

We consider a straight beam of length $L = 4\,\mathrm{m}$ and square cross-section of side $t = 0.2\,\mathrm{m}$, lying along the x_1-axis. The beam is clamped at one end, and it is loaded with an axial force F_1 at the free end. Two different hyperelastic materials are considered: Saint Venant-Kirchhoff (SVK) and compressible Neo-Hookean (NH), characterized by the following strain energy functions

$$\psi_{\mathrm{SVK}} = \frac{1}{2}\gamma(\mathrm{tr}\mathbf{E})^2 + \mu\mathbf{E} : \mathbf{E} \quad \text{and} \quad \psi_{\mathrm{NH}} = \frac{E}{2}(\mathrm{tr}\mathbf{E} - \ln J), \tag{39}$$

where $\gamma = \frac{E\nu}{(1+\nu)(1-2\nu)}$ and $\mu = \frac{E}{2(1+\nu)}$ are the so-called Lamè elastic constant, while $J = \sqrt{\det(\mathbf{C})} = \det(\mathbf{F})$ is the Jacobian of the deformation gradient. For these strain energy functions, the exact value of the displacement along x_1 under finite strains can be found solving analytically the following nonlinear equations [89]

$$\frac{u_{\mathrm{SVK}}^3}{L^2} + \frac{3u_{\mathrm{SVK}}^2}{L} + 2u_{\mathrm{SVK}} - \frac{2F_1L}{EA} = 0, \qquad u_{\mathrm{NH}}^2 + u_{\mathrm{NH}}\left(2L - \frac{2F_1L}{EA}\right) - \frac{2F_1L^2}{EA} = 0, \tag{40}$$

where $A = t^2$ is the area of the beam cross-section. We remark that, among the roots of the above equations, only one is admissible with the imposed load conditions.

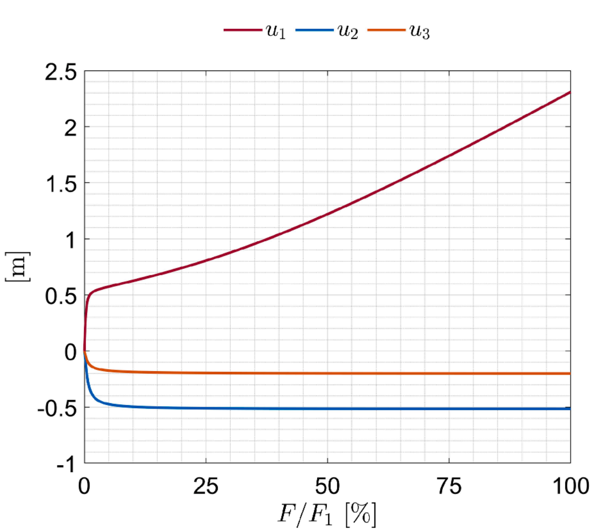

(a) Tip displacement components vs load increment.

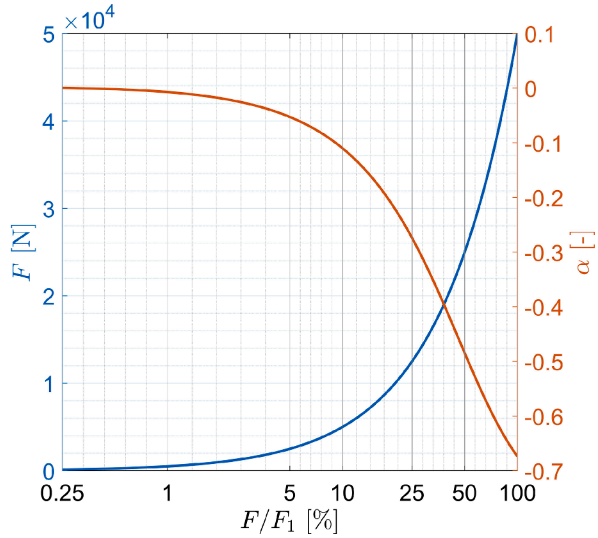

(b) Load intensity (left) and area dilatation (right).

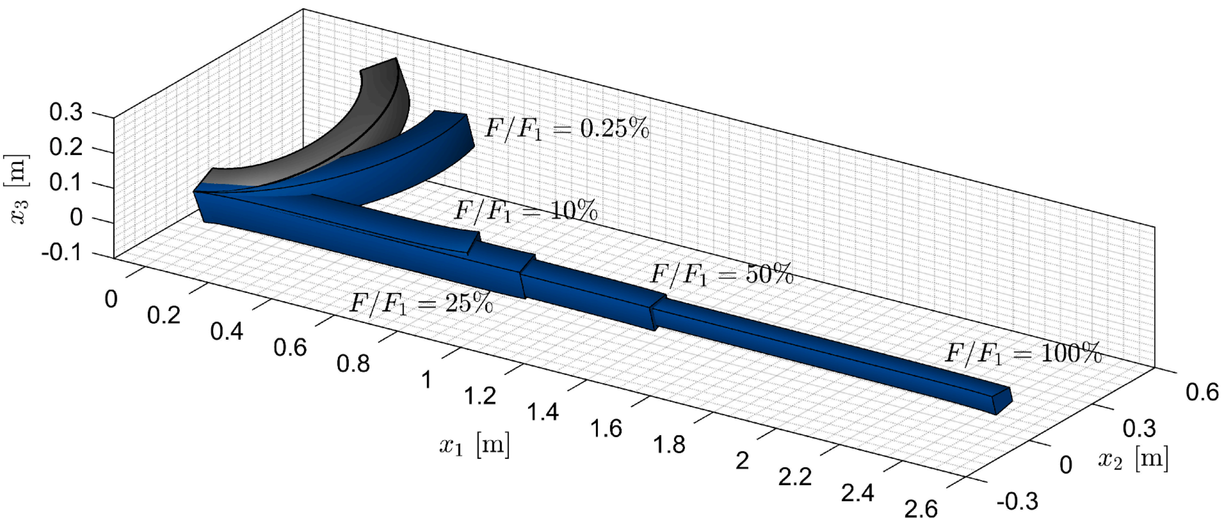

(c) Deformed snapshots (solid blue) at relevant load increments; solid grey refers to the initial configuration.

Fig. 7. Straightening of a circular arch: displacement components, load intensity and area dilatation ratio vs load increment (top); deformed configurations (bottom).

For the numerical solutions, we adopt $\mathrm{n} = 40$ collocation points and B-Spline basis functions of degree $p = 4$. Results are presented in Fig. 2, where the magnitude of the applied force, F_1, is plotted against the axial displacement u_1. Blue solid lines refer to the analytical solutions, while orange circles refer to the numerical results. The nonlinear force-displacement relationships are clearly noticeable, with different behaviour in tension and compression, for both SVK (Fig. 2(a)) and NH (Fig. 2(b)).

Overall, an excellent agreement with the analytical solution is achieved.

5.2. Compressible Neo-Hookean material: uniaxial tensile test

We further check the proposed formulation with an uniaxial tensile test, where a compressible NH material with $\nu \neq 0$ is considered. The scope of this benchmark test is to assess the capability of the method to accurately predict the in-plane cross-sectional strains, $\mathbf{E}_z$.

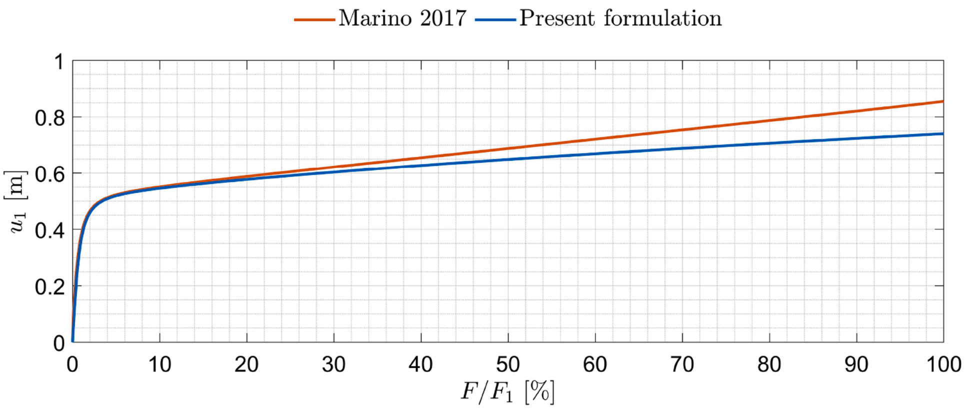

Fig. 8. Straightening of a circular arch made of SVK material under $F_1 = 2 \times 10^4$ N: tip displacement along x_1 vs load increment. Comparison between Marino 2017 [62] and the present formulation..

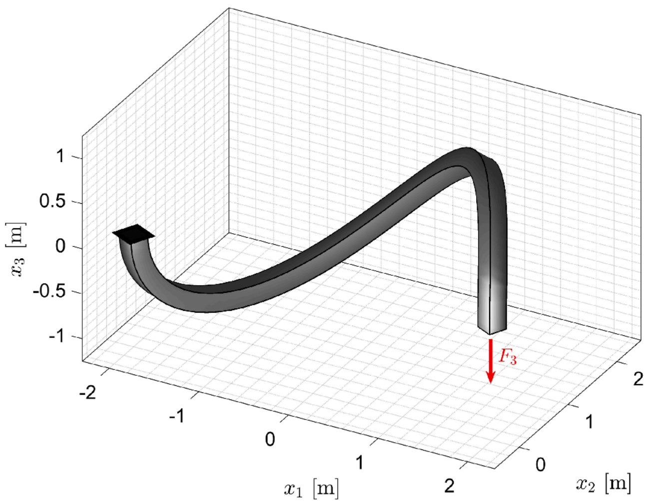

(a) 3D view.

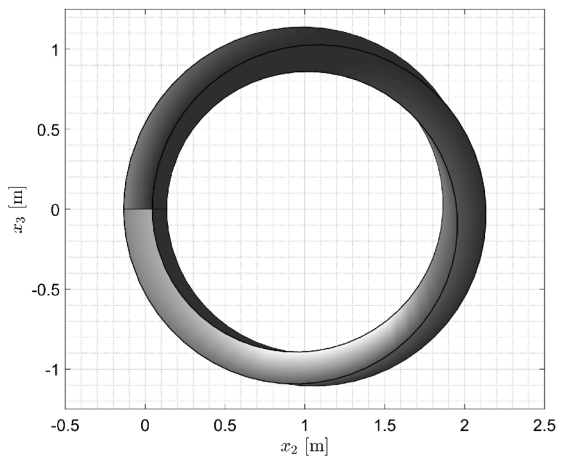

(b) Planar (x_2, x_3) view.

Fig. 9. Viviani beam: initial configuration.

The beam features a length of $L = 1$ m and a square cross-section of side 0.1×0.1m. We employ a strain energy function defined as

$$\psi_{\mathrm{NH}} = \frac{\mu}{2}\left(\det(\mathbf{C})^{-1/3}\mathrm{tr}(\mathbf{C}) - 3\right) + \frac{1}{4}K\left(\det(\mathbf{C}) - 1 - \ln(\det(\mathbf{C}))\right), \tag{41}$$

where $K = 2\mu(1+\nu)/(3-6\nu)$ is the bulk modulus. As material parameters, we adopt $\mu = 1.5 \times 10^6$ N/m^2 and different values for the Poisson's coefficient $\nu = \{0.40, 0.45, 0.49, 0.49999\}$.

For this particular application, the principal stretches, λ_β, $\beta = 2, 3$, can be computed analytically as [60]

$$\lambda_2 = \lambda_3 = \sqrt{\frac{J}{\lambda}}, \tag{42}$$

with $\lambda = \lambda_1$. Enforcing the plane stress equilibrium $\sigma_{22} = \sigma_{33} = 0$, the following relationship between J and λ is obtained

$$-\frac{1}{3}\mu J^{-5/3}\left(\lambda^2 - \frac{J}{\lambda}\right) + \frac{1}{2}K\left(J - \frac{1}{J}\right) = 0\,. \tag{43}$$

Solving the above equation for J for different values of λ permits also computing in a closed form the Cauchy stress component, σ_{11}, as

$$\sigma_{11} = \mu J^{-5/3}\left(\lambda^2 - \frac{J}{\lambda}\right). \tag{44}$$

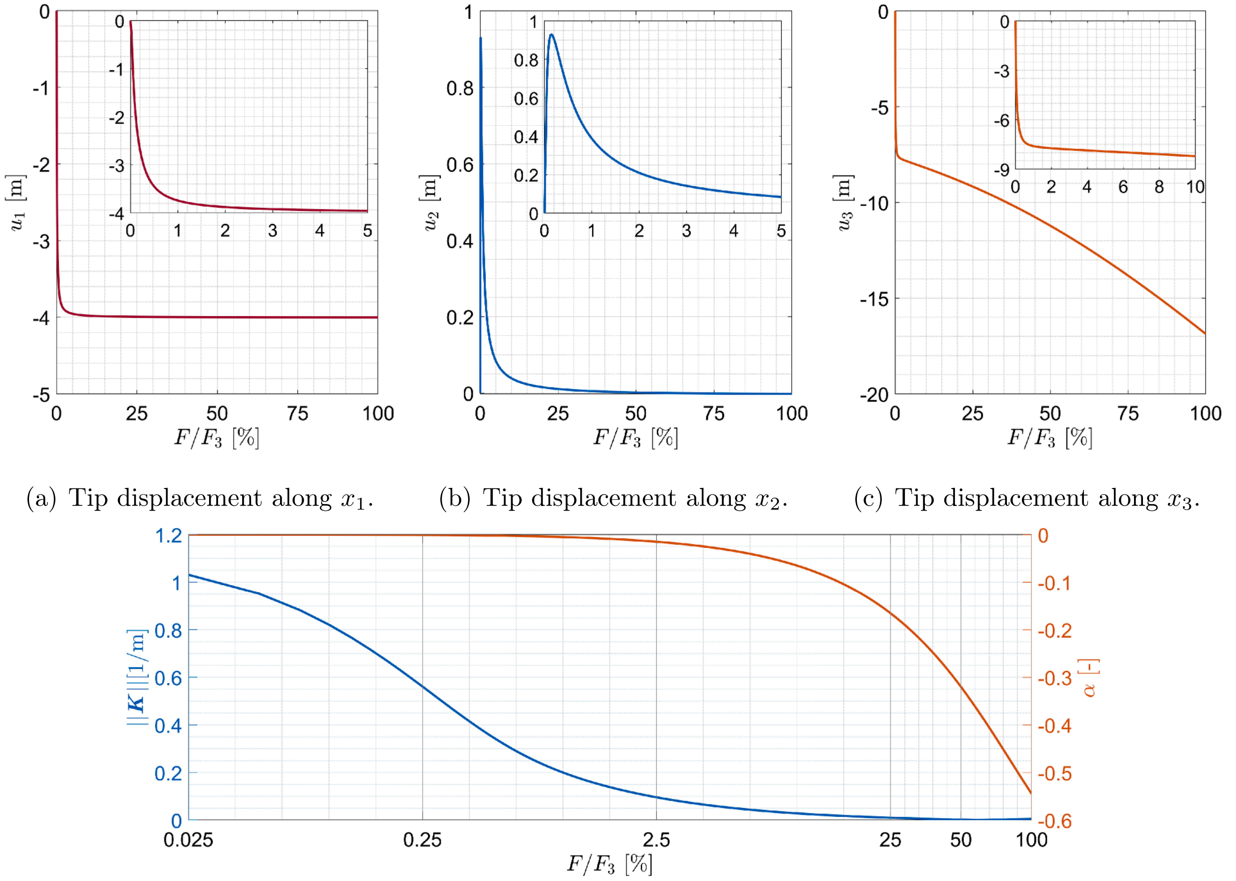

(a) Tip displacement along x_1. (b) Tip displacement along x_2. (c) Tip displacement along x_3.

(d) $||\boldsymbol{K}||$ at the clamped end (blue), $\boldsymbol{\alpha}$ at the free end (orange) vs load increment.

Fig. 10. Viviani beam: tip displacement components (a-c) vs load increment; norm of the material curvature and area dilatation (d) vs load increment.

We check the numerical results with the analytical solutions, imposing an axial force, $F_1 = 1 \times 10^5$ N. The comparison is carried in terms of the axial Cauchy stress, σ_{11}, and in terms of area dilatation ratio $\alpha = (A - A_0)/A_0$. The latter is computed in the numerical model defining the deformed area as

$$A = A_0 \lambda_2 \lambda_3, \tag{45}$$

where the cross-sectional stretches are defined as $\lambda_\beta = \sqrt{2\mathrm{E}_{\beta\beta} + 1}$ [90].

Fig. 3 shows the comparison between the analytical and numerical solutions. Different curves are associated with a different value of ν. Fig. 3(a) shows the axial stress, σ_{11}, as a function of λ, whereas the area dilatation ratio, α is plotted in Fig. 3(b). An excellent agreement with the analytical results is achieved for both quantities.

Extruded view for NH materials with $\nu = 0.4$ (blue) and $\nu = 0.49999$ (orange) at $\lambda \simeq 6$ are shown in Fig. 4, proving the capability of the method to simulate the cross-sectional contraction, at such large strains: the beam length increases of about six times its initial value.

5.3. Circular arch subjected to an out-of plane tip force

In order to test the ability in simulating curved beams, we study a 45 ° circular arch loaded by an out-of-plane force. The beam lies in the (x_1, x_2) plane. The structure is clamped at one end and loaded with a force along the x_3-direction, $F_3 = 2000$ N. The beam centroid features a radius $R = 1$ m and a square cross-section of side $t = 0.1$ m. We consider a NH material with $\mu = 1.5 \times 10^6$ N/m^2, $\nu = 0.3$, and ψ_{NH} defined in Eq. (41). In Fig. 5(a), we show the extruded view of the undeformed (grey) and final, deformed, configurations (blue).

We verify that higher-order convergence rates are preserved by comparing the displacements evaluated over a fixed grid of points, $\boldsymbol{u}^h$, with respect to the ones of a reference solution, $\boldsymbol{u}^r$, obtained with $p = 8$ and 100 collocation points. The L_2 norm of the error on the displacement vector, $err_{L_2} = ||\boldsymbol{u}^r - \boldsymbol{u}^h||/||\boldsymbol{u}^r||$, is presented in Fig. 5(b), for $p = 2$, 4, 6 degree of NURBS basis functions vs. the

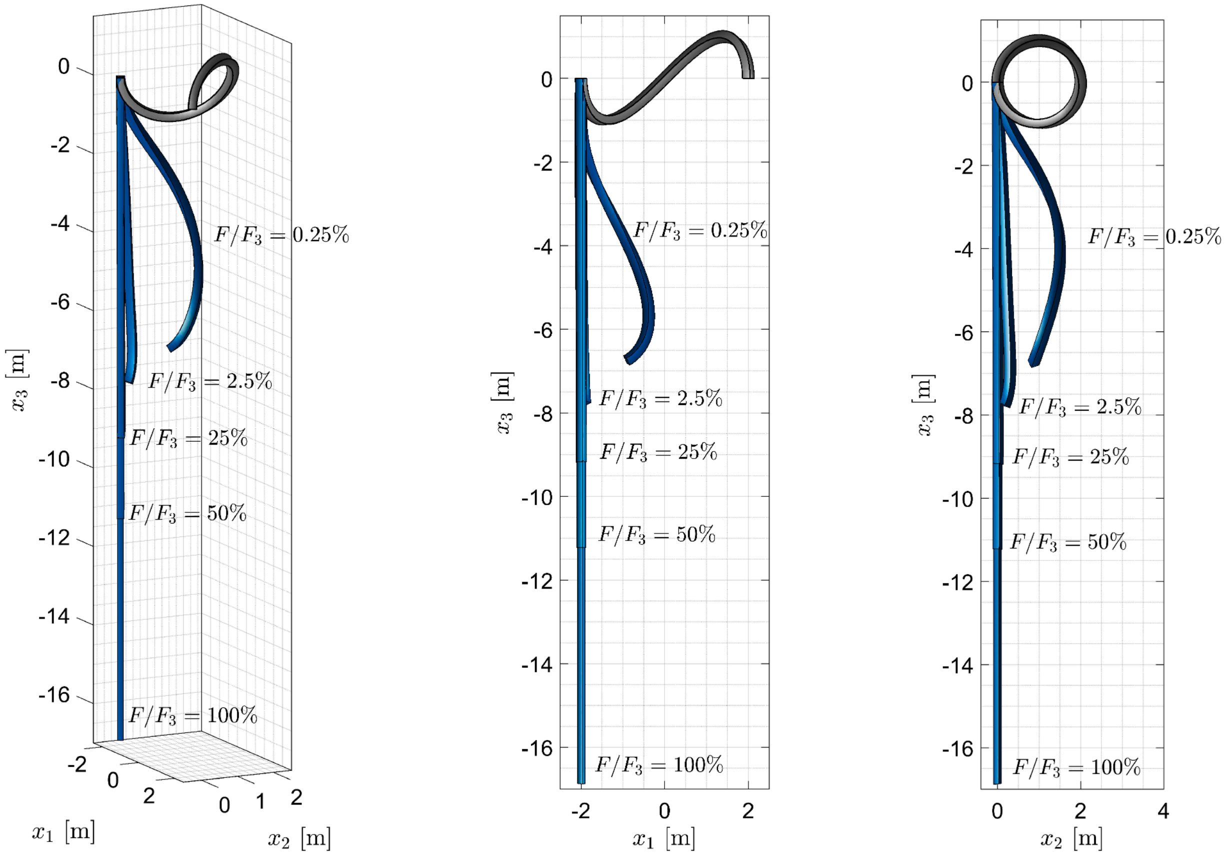

(a) 3D view.
(b) Planar (x_1, x_3) view.
(c) Planar (x_2, x_3) view.

Fig. 11. Viviani beam: deformed configuration snapshots (solid blue) at relevant load steps; solid grey refers to the initial configuration. (For interpretation of the references to colour in this figure legend, the reader is referred to the web version of this article.)

number of collocation points. As it is well known for IGA-C, odd degrees do not normally improve the rates compared to the smaller even degrees, therefore they are not considered. As it can be seen, results are in excellent agreement with the expected rates (see dashed lines in Fig. 5(b)).

5.4. Straightening of a circular arch at large strains

This numerical example concerns a 135°-circular arch of radius $R = 4/(3\sqrt{2}\pi)$m (see Fig. 6), clamped at its bottom end, $x_3 = 0$, straightened along x_1 by a force, $F_1 = 5 \times 10^4$ N, applied at the top free end. This test is meant to show the most important attribute of the proposed model, namely the ability to capture at the same time both finite deformations and finite strains. The exact geometry of the beam centroid is reconstructed using $p = 2$ NURBS basis functions with the control points, $\check{\boldsymbol{p}}_j$, $j = 1, 2, 3$, and weights, w, shown in Table 1 [91], and then discretized with $p = 4$ and $\mathrm{n} = 60$. The beam features a square cross-section of side $t = 0.1$ m. A NH material with $\mu = 1.5 \times 10^6$ N/m^2 and $\nu = 0.49999$ is considered.

Results are shown in Fig. 7. The beam is almost straightened with a load equal to $10\,\%F_1$. From that load intensity on, the displacements along x_2 and x_3 reach asymptotic values (see Fig. 7(a)), whereas u_1 keeps increasing. Area dilatation ratio, α, is plotted with the load intensity in Fig. 7(b). Here, the load increment is plotted in logarithmic scale to capture the progressive cross-sectional shrinkage starting from $10\,\%F_1$, once the beam is straightened along x_1. This behaviour can be clearly seen also in Fig. 7(c).

To further investigate the finite strain effects, the circular arch is now considered made of a SVK material with strain energy function defined in Eq. (39). Load intensity is set to $F_1 = 2 \times 10^4$ N. Results are compared with the ones obtained with a small strain formulation [62]. Fig. 8 shows the tip displacement component along the axis x_1 vs. the load intensity. It can be seen that, in cases of large deformation only (see up to 10 % of loading), results associated with the two formulations almost coincide since finite strain effects are negligible. From a load intensity of approximately $10\,\%F_1$, namely when a straight configuration is reached, the beam starts undergoing finite strains with a significant cross-sectional shrinking, which results in an axial stiffening.

5.5. The viviani beam

The Viviani beam is a challenging curved beam [92]. The beam centroid is defined by the curve $\boldsymbol{c}(s) = [2a\sin(s/2),\, a(1+\cos(s)),\, a\sin(s)]^{\mathsf{T}}$, with $a = 10$ and $s \in [-\pi, \pi]$ (see Fig. 9).

The beam is clamped at one end, and loaded by a force $F_3 = -1.2 \times 10^5$ N applied at its free end and directed along x_3. It features a square cross-section of side 0.2 m. The same NH material used in the above tests is here adopted. The beam centroid is discretized with $p = 4$ B-Splines and $\mathrm{n} = 60$ collocation points.

Results in terms of tip displacement are shown in Figs. 10(a)- 10(c), whereas the norm of curvature (in the material form) at the clamped end (blue solid line) is plotted in Fig. 10(d) together with the area dilatation ratio at the tip of beam (orange solid line). Compared to the previous test, the beam is almost completely straightened with 2.5 % of the final load, with curvature dropping of more than 80 % compared to its initial value (Fig. 10(d)). On the other end, the cross-section shrinkage is still very small but rapidly increases reaching a reduction of more than 50 % compared to the initial undeformed cross-section as the load reaches its maximum.

Finally, deformation snapshots at some significant load increments are shown in Fig. 11, where it is possible to see how the beam undergoes large deformations and strains.

6. Conclusions

In this paper, we proposed a finite strain geometrically exact beam formulation for general hyperelastic materials. Keeping the shear-deformable kinematic assumption, we provided the relationship between the beam strain measures and the Cauchy-Green tensor components. Constitutive relationships are obtained starting form the hyperelastic strain energy and integrating the second Piola-Kirchhoff stress vector over the undeformed beam cross-section. The linearization of the beam stress-strain relationships is done adopting the local plane-stress algorithm proposed in [59]. This allows to obtain the elasticity tangent tensor, and to compute the in-plane strain components, required for the calculation of the beam cross-sectional deformations without any modification of the beam kinematics and with no additional unknowns. The set of governing equations is completed by the balance equations in the local form. To further improve efficiency while keeping high accuracy, spatial discretization is made by means of the Isogeometric Collocation (IGA-C) method. We assessed the capabilities of the proposed approach through a series of numerical experiments covering all the distinguishing features of the formulation, and in particular the capability to reproduce both large deformations and finite strains occurring at the same time. Given the generality of the method, ongoing research is focused on extending the formulation to other nonlinear and rate–dependent constitutive models.

CRediT authorship contribution statement

Diego Ignesti: Writing – review & editing, Writing - original draft, Visualization, Validation, Software, Methodology, Investigation, Formal analysis, Data curation, Conceptualization; **Giulio Ferri:** Writing – review & editing, Writing - original draft, Visualization, Validation, Software, Methodology, Investigation, Formal analysis, Data curation, Conceptualization; **Alessandro Reali:** Writing – review & editing, Supervision, Methodology, Investigation, Formal analysis, Conceptualization; **Ferdinando Auricchio:** Writing – review & editing, Supervision, Methodology, Investigation, Formal analysis, Conceptualization; **Josef Kiendl:** Writing – review & editing, Supervision, Software, Methodology, Investigation, Formal analysis, Conceptualization; **Enzo Marino:** Writing – review & editing, Writing - original draft, Supervision, Resources, Methodology, Investigation, Funding acquisition, Formal analysis, Conceptualization.

Data availability

Data will be made available on request.

Declaration of competing interest

The authors declare that they have no known competing financial interests or personal relationships that could have appeared to influence the work reported in this paper.

Acknowledgement

EM was partially supported by the European Union - Next Generation EU, in the context of The National Recovery and Resilience Plan, Investment 1.5 Ecosystems of Innovation, Project Tuscany Health Ecosystem (THE). (CUP: B83C22003920001).

EM was partially supported by the National Centre for HPC, Big Data and Quantum Computing funded by the European Union within the Next Generation EU recovery plan. (CUP B83C22002830001).

EM and GF were partially supported by the UniFI project IGA4Stent - “Patient-tailored stents: an innovative computational iso-geoemtric analysis approach for 4D printed shape changing devices”. (CUP B55F21007810001).

EM and DI were partially supported by the PRIN 2022 project NonlinEar Phenomena in floaTing offshore wind tUrbiNEs (NEP-TUNE), prot. 2022W7SKTL. (CUP B53D23006480006), funded by the Italian MUR.

JK was supported by the European Research Council (ERC) under the European 428 Union’s Horizon 2020 research and innovation programme (grant agreement No 864482). These supports are gratefully acknowledged.

Appendix A

According to the beam theory, the stress components S^{22}, S^{33} and S^{23} are assumed to be zero [30]. To adapt the stress-strain relationship to this specific stress condition, we use the algorithm proposed in [59], which is briefly recalled here. Eq. (16) is rewritten in a partitioned form

$$\begin{bmatrix}\partial\mathbf{S}_m\\ \partial\mathbf{S}_z\end{bmatrix}=\begin{bmatrix}\mathbb{C}_{mm} & \mathbb{C}_{mz}\\ \mathbb{C}_{zm} & \mathbb{C}_{zz}\end{bmatrix}\begin{bmatrix}\partial\mathbf{E}_m\\ \partial\mathbf{E}_z\end{bmatrix}. \tag{46}$$

Enforcing the condition $\partial \boldsymbol{S}_z=\mathbf{0}$ permits expressing $\partial\mathbf{E}_z$ as

$$\partial\mathbf{E}_z=-\mathbb{C}_{zz}^{-1}\mathbb{C}_{zm}\partial\mathbf{E}_m, \tag{47}$$

whereas the non-zero values of the incremental stress components are given by

$$\partial\mathbf{S}_m=\mathbb{C}_{mm}\partial\mathbf{E}_m+\mathbb{C}_{mz}\partial\mathbf{E}_z\,. \tag{48}$$

Substituting Eq. (47) into (48) leads to

$$\partial\mathbf{S}_m=\mathbb{C}_{up}\partial\mathbf{E}_m, \tag{49}$$

where

$$\mathbb{C}_{up}=[\mathbb{C}_{mm}-\mathbb{C}_{mz}\mathbb{C}_{zz}^{-1}\mathbb{C}_{zm}] \tag{50}$$

is the (3×3) beam-adapted tangent modulus. Note that $\mathbf{S}_m$ depends only on $\mathbf{E}_m$. We further observe that, for an incompressible material, $\mathbb{C}_{up}$ can be defined analytically, while for compressible materials it must be computed iteratively, as well as $\mathbf{E}_z$ [60].

Appendix B

From the linearized version of the internal force supplementary equations, Eqs. (30) and (31), we have the following integral quantities

$$\begin{aligned}\hat{\boldsymbol{T}}_{\eta\eta}=\int_{A_0}&\mathbf{R}_0\hat{\boldsymbol{\Gamma}}_N\hat{\mathbb{C}}_{up}^{1l}\hat{\mathbf{A}}\boldsymbol{C}\hat{\mathbf{R}}^{\mathsf{T}}+\hat{\mathbb{S}}^{11}\boldsymbol{C}\mathbf{R}_0\hat{\mathbf{R}}^{\mathsf{T}}+\mathbf{R}_0\hat{\boldsymbol{K}}_\xi\hat{\mathbb{C}}_{up}^{1l}\hat{\mathbf{A}}\boldsymbol{C}\hat{\mathbf{R}}^{\mathsf{T}}+\boldsymbol{D}_1\hat{\mathbb{C}}_{up}^{1l}\hat{\mathbf{A}}\boldsymbol{C}^2\hat{\mathbf{R}}^{\mathsf{T}}+\\&-\boldsymbol{D}_2 s_3 K_{01}\hat{\mathbb{C}}_{up}^{1l}\hat{\mathbf{A}}\boldsymbol{C}\hat{\mathbf{R}}^{\mathsf{T}}+\boldsymbol{D}_3 s_2 K_{01}\hat{\mathbb{C}}_{up}^{1l}\hat{\mathbf{A}}\boldsymbol{C}\hat{\mathbf{R}}^{\mathsf{T}}+\boldsymbol{D}_2\hat{\mathbb{C}}_{up}^{2l}\hat{\mathbf{A}}\boldsymbol{C}\hat{\mathbf{R}}^{\mathsf{T}}+\boldsymbol{D}_3\hat{\mathbb{C}}_{up}^{3l}\hat{\mathbf{A}}\boldsymbol{C}\hat{\mathbf{R}}^{\mathsf{T}}\,dA_0,\end{aligned} \tag{51}$$

being the integral associated with the translational unknown (second subscript η),

$$\begin{aligned}\hat{\boldsymbol{T}}_{\eta\vartheta}^1=\int_{A_0}&\hat{\mathbb{S}}^{11}\boldsymbol{C}\mathbf{R}_0\hat{\boldsymbol{\Gamma}}_N+\hat{\mathbb{S}}^{11}\boldsymbol{C}\mathbf{R}_0\hat{\boldsymbol{K}}_\xi+\hat{\mathbb{S}}^{11}\boldsymbol{C}^2\boldsymbol{D}_1-s_3K_{01}\hat{\mathbb{S}}^{11}\boldsymbol{C}\boldsymbol{D}_2+s_2K_{01}\hat{\mathbb{S}}^{11}\boldsymbol{C}\boldsymbol{D}_3+\\&+\hat{\mathbb{S}}^{21}\boldsymbol{C}\boldsymbol{D}_2+\hat{\mathbb{S}}^{31}\boldsymbol{C}\boldsymbol{D}_3\,dA_0,\end{aligned} \tag{52}$$

$$\begin{aligned}\hat{\boldsymbol{T}}_{\eta\vartheta}^2=\int_{A_0}&\mathbf{R}_0\hat{\boldsymbol{\Gamma}}_N\hat{\mathbb{C}}_{up}^{1l}\hat{\mathbf{A}}\boldsymbol{C}\hat{\mathbf{R}}^{\mathsf{T}}\hat{\boldsymbol{c}}_{,s}+\hat{\mathbb{S}}^{11}\boldsymbol{C}\mathbf{R}_0\hat{\mathbf{R}}^{\mathsf{T}}\hat{\boldsymbol{c}}_{,s}+\mathbf{R}_0\hat{\boldsymbol{K}}_\xi\hat{\mathbb{C}}_{up}^{1l}\hat{\mathbf{A}}\boldsymbol{C}\hat{\mathbf{R}}^{\mathsf{T}}\hat{\boldsymbol{c}}_{,s}+\\&+\boldsymbol{D}_1\hat{\mathbb{C}}_{up}^{1l}\hat{\mathbf{A}}\boldsymbol{C}^2\hat{\mathbf{R}}^{\mathsf{T}}\hat{\boldsymbol{c}}_{,s}-\boldsymbol{D}_2s_3K_{01}\hat{\mathbb{C}}_{up}^{1l}\hat{\mathbf{A}}\boldsymbol{C}\hat{\mathbf{R}}^{\mathsf{T}}\hat{\boldsymbol{c}}_{,s}+\boldsymbol{D}_3s_2K_{01}\hat{\mathbb{C}}_{up}^{1l}\hat{\mathbf{A}}\boldsymbol{C}\hat{\mathbf{R}}^{\mathsf{T}}\hat{\boldsymbol{c}}_{,s}+\\&+\boldsymbol{D}_2\hat{\mathbb{C}}_{up}^{2l}\hat{\mathbf{A}}\boldsymbol{C}\hat{\mathbf{R}}^{\mathsf{T}}\hat{\boldsymbol{c}}_{,s}+\boldsymbol{D}_3\hat{\mathbb{C}}_{up}^{3l}\hat{\mathbf{A}}\boldsymbol{C}\hat{\mathbf{R}}^{\mathsf{T}}\hat{\boldsymbol{c}}_{,s}\,dA_0,\end{aligned} \tag{53}$$

$$\begin{aligned}\hat{\boldsymbol{T}}_{\eta\vartheta}^3=\int_{A_0}&\mathbf{R}_0\hat{\boldsymbol{\Gamma}}_N\hat{\mathbb{C}}_{up}^{1l}\hat{\mathbf{B}}\boldsymbol{C}\hat{\mathbf{R}}^{\mathsf{T}}+\mathbf{R}_0\hat{\boldsymbol{K}}_\xi\hat{\mathbb{C}}_{up}^{1l}\hat{\mathbf{B}}\boldsymbol{C}\hat{\mathbf{R}}^{\mathsf{T}}-s_2\hat{\mathbb{S}}^{11}\boldsymbol{C}\mathbf{R}_0\hat{\mathbf{R}}^{\mathsf{T}}(\widetilde{\hat{\mathbf{R}}\boldsymbol{E}_2})+\\&-s_3\hat{\mathbb{S}}^{11}\boldsymbol{C}\mathbf{R}_0\hat{\mathbf{R}}^{\mathsf{T}}(\widetilde{\hat{\mathbf{R}}\boldsymbol{E}_3})+\boldsymbol{D}_1\hat{\mathbb{C}}_{up}^{1l}\hat{\mathbf{B}}\boldsymbol{C}^2\hat{\mathbf{R}}^{\mathsf{T}}-\boldsymbol{D}_2s_3K_{01}\hat{\mathbb{C}}_{up}^{1l}\hat{\mathbf{B}}\boldsymbol{C}\hat{\mathbf{R}}^{\mathsf{T}}+\\&+\boldsymbol{D}_3s_2K_{01}\hat{\mathbb{C}}_{up}^{1l}\hat{\mathbf{B}}\boldsymbol{C}\hat{\mathbf{R}}^{\mathsf{T}}+\boldsymbol{D}_2\hat{\mathbb{C}}_{up}^{2l}\hat{\mathbf{B}}\boldsymbol{C}\hat{\mathbf{R}}^{\mathsf{T}}+\boldsymbol{D}_3\hat{\mathbb{C}}_{up}^{3l}\hat{\mathbf{B}}\boldsymbol{C}\hat{\mathbf{R}}^{\mathsf{T}}\,dA_0,\end{aligned} \tag{54}$$

that are the integral quantities associated with the incremental rotations (second subscript ϑ), and

$$\begin{aligned}\hat{\boldsymbol{T}}_n=\int_{A_0}&\hat{\mathbb{S}}^{11}\boldsymbol{C}\mathbf{R}_0\hat{\boldsymbol{\Gamma}}_N+\hat{\mathbb{S}}^{11}\boldsymbol{C}\mathbf{R}_0\hat{\boldsymbol{K}}_\xi+\hat{\mathbb{S}}^{11}\boldsymbol{C}^2\boldsymbol{D}_1-s_3K_{01}\hat{\mathbb{S}}^{11}\boldsymbol{C}\boldsymbol{D}_2+s_2K_{01}\hat{\mathbb{S}}^{11}\boldsymbol{C}\boldsymbol{D}_3+\\&+\hat{\mathbb{S}}^{21}\boldsymbol{C}\boldsymbol{D}_2+\hat{\mathbb{S}}^{31}\boldsymbol{C}\boldsymbol{D}_3\,dA_0\,,\end{aligned} \tag{55}$$

that is associated with the current internal forces (subscript n).

Similarly, we have defined

$$\begin{aligned}\hat{\boldsymbol{T}}_{\vartheta\eta}=\int_{A_0}(s_2\widetilde{\boldsymbol{D}_2+s_3}\boldsymbol{D}_3)\Big(&\mathbf{R}_0\hat{\boldsymbol{\Gamma}}_N\hat{\mathbb{C}}_{up}^{1l}\hat{\mathbf{A}}\boldsymbol{C}\hat{\mathbf{R}}^{\mathsf{T}}+\hat{\mathbb{S}}^{11}\boldsymbol{C}\mathbf{R}_0\hat{\mathbf{R}}^{\mathsf{T}}+\mathbf{R}_0\hat{\boldsymbol{K}}_\xi\hat{\mathbb{C}}_{up}^{1l}\hat{\mathbf{A}}\boldsymbol{C}\hat{\mathbf{R}}^{\mathsf{T}}+\\&+\boldsymbol{D}_1\hat{\mathbb{C}}_{up}^{1l}\hat{\mathbf{A}}\boldsymbol{C}^2\hat{\mathbf{R}}^{\mathsf{T}}-\boldsymbol{D}_2s_3K_{01}\hat{\mathbb{C}}_{up}^{1l}\hat{\mathbf{A}}\boldsymbol{C}\hat{\mathbf{R}}^{\mathsf{T}}+\boldsymbol{D}_3s_2K_{01}\hat{\mathbb{C}}_{up}^{1l}\hat{\mathbf{A}}\boldsymbol{C}\hat{\mathbf{R}}^{\mathsf{T}}+\\&+\boldsymbol{D}_2\hat{\mathbb{C}}_{up}^{2l}\hat{\mathbf{A}}\boldsymbol{C}\hat{\mathbf{R}}^{\mathsf{T}}+\boldsymbol{D}_3\hat{\mathbb{C}}_{up}^{3l}\hat{\mathbf{A}}\boldsymbol{C}\hat{\mathbf{R}}^{\mathsf{T}}\Big)dA_0,\end{aligned} \tag{56}$$

$$\hat{\boldsymbol{T}}^1_{\vartheta\vartheta} = \int_{A_0} (s_2\widetilde{\boldsymbol{D}_2 + s_3}\boldsymbol{D}_3)\Big(\hat{\mathrm{S}}^{11}C\mathbf{R}_0\hat{\boldsymbol{\Gamma}}_N + \hat{\mathrm{S}}^{11}C\mathbf{R}_0\hat{\boldsymbol{K}}_\xi + \hat{\mathrm{S}}^{11}C^2\boldsymbol{D}_1 - s_3K_{01}\hat{\mathrm{S}}^{11}C\boldsymbol{D}_2 + \\ + s_2K_{01}\hat{\mathrm{S}}^{11}C\boldsymbol{D}_3 + \hat{\mathrm{S}}^{21}C\boldsymbol{D}_2 + \hat{\mathrm{S}}^{31}C\boldsymbol{D}_3\Big)dA_0, \tag{57}$$

and

$$\hat{\boldsymbol{T}}^2_{\vartheta\vartheta} = \int_{A_0} (s_2\widetilde{\boldsymbol{D}_2 + s_3}\boldsymbol{D}_3)\Big(\mathbf{R}_0\hat{\boldsymbol{\Gamma}}_N\hat{\mathbb{C}}^{1l}_{up}\hat{\mathbf{A}}C\hat{\mathbf{R}}^{\mathsf{T}}\hat{\widetilde{\boldsymbol{c}}},_s + \hat{\mathrm{S}}^{11}C\mathbf{R}_0\hat{\mathbf{R}}^{\mathsf{T}}\hat{\widetilde{\boldsymbol{c}}},_s + \\ + \mathbf{R}_0\hat{\boldsymbol{K}}_\xi\hat{\mathbb{C}}^{1l}_{up}\hat{\mathbf{A}}C\hat{\mathbf{R}}^{\mathsf{T}}\hat{\widetilde{\boldsymbol{c}}},_s + \boldsymbol{D}_1\hat{\mathbb{C}}^{1l}_{up}\hat{\mathbf{A}}C^2\hat{\mathbf{R}}^{\mathsf{T}}\hat{\widetilde{\boldsymbol{c}}},_s - \boldsymbol{D}_2s_3K_{01}\hat{\mathbb{C}}^{1l}_{up}\hat{\mathbf{A}}C\hat{\mathbf{R}}^{\mathsf{T}}\hat{\widetilde{\boldsymbol{c}}},_s + \\ + \boldsymbol{D}_3s_2K_{01}\hat{\mathbb{C}}^{1l}_{up}\hat{\mathbf{A}}C\hat{\mathbf{R}}^{\mathsf{T}}\hat{\widetilde{\boldsymbol{c}}},_s + \boldsymbol{D}_2\hat{\mathbb{C}}^{2l}_{up}\hat{\mathbf{A}}C\hat{\mathbf{R}}^{\mathsf{T}}\hat{\widetilde{\boldsymbol{c}}},_s + \boldsymbol{D}_3\hat{\mathbb{C}}^{3l}_{up}\mathbf{A}C\hat{\mathbf{R}}^{\mathsf{T}}\hat{\widetilde{\boldsymbol{c}}},_s \Big)dA_0, \tag{58}$$

$$\hat{\boldsymbol{T}}^3_{\vartheta\vartheta} = \int_{A_0} (s_2\widetilde{\boldsymbol{D}_2 + s_3}\boldsymbol{D}_3)\Big(\mathbf{R}_0\hat{\boldsymbol{\Gamma}}_N\hat{\mathbb{C}}^{1l}_{up}\hat{\mathbf{B}}C\hat{\mathbf{R}}^{\mathsf{T}} + \mathbf{R}_0\hat{\boldsymbol{K}}_\xi\hat{\mathbb{C}}^{1l}_{up}\hat{\mathbf{B}}C\hat{\mathbf{R}}^{\mathsf{T}} + \\ - s_2\hat{\mathrm{S}}^{11}C\mathbf{R}_0\hat{\mathbf{R}}^{\mathsf{T}}(\widetilde{\hat{\mathbf{R}}\boldsymbol{E}_2}) - s_3\hat{\mathrm{S}}^{11}C\mathbf{R}_0\hat{\mathbf{R}}^{\mathsf{T}}(\widetilde{\hat{\mathbf{R}}\boldsymbol{E}_3}) + \boldsymbol{D}_1\hat{\mathbb{C}}^{1l}_{up}\hat{\mathbf{B}}C^2\hat{\mathbf{R}}^{\mathsf{T}} + \\ + \boldsymbol{D}_2(\hat{\mathbb{C}}^{2l}_{up}\hat{\mathbf{B}}C\hat{\mathbf{R}}^{\mathsf{T}} - s_3K_{01}\hat{\mathbb{C}}^{1l}_{up}\hat{\mathbf{B}}C\hat{\mathbf{R}}^{\mathsf{T}}) + \boldsymbol{D}_3(\hat{\mathbb{C}}^{3l}_{up}\hat{\mathbf{B}}C\hat{\mathbf{R}}^{\mathsf{T}} + s_2K_{01}\hat{\mathbb{C}}^{1l}_{up}\hat{\mathbf{B}}C\hat{\mathbf{R}}^{\mathsf{T}}) \Big)dA_0, \tag{59}$$

$$\hat{\boldsymbol{T}}_m = \int_{A_0} (s_2\widetilde{\boldsymbol{D}_2 + s_3}\boldsymbol{D}_3)\Big(\hat{\mathrm{S}}^{11}C\mathbf{R}_0\hat{\boldsymbol{\Gamma}}_N + \hat{\mathrm{S}}^{11}C\mathbf{R}_0\hat{\boldsymbol{K}}_\xi + \hat{\mathrm{S}}^{11}C^2\boldsymbol{D}_1 - s_3K_{01}\hat{\mathrm{S}}^{11}C\boldsymbol{D}_2 + \\ + s_2K_{01}\hat{\mathrm{S}}^{11}C\boldsymbol{D}_3 + \hat{\mathrm{S}}^{21}C\boldsymbol{D}_2 + \hat{\mathrm{S}}^{31}C\boldsymbol{D}_3\Big)dA_0, \tag{60}$$

that are the integral quantities appearing in the linearized version of the internal couples supplementary equation, Eqs. (31).

The values $\hat{\mathbb{C}}^{1l}_{up}$, $\hat{\mathbb{C}}^{2l}_{up}$ and $\hat{\mathbb{C}}^{3l}_{up}$, $l = 1, 2, 3$, are first, second and third rows of the adapted tangent modulus, $\hat{\mathbb{C}}_{up}$ (see Eq. (50)), appearing in the linearization of each stress component S^{k1}, $k = 1, 2, 3$, with respect to the strain components, E^{1l},

$$\mathbb{C}^{kl}_{up} = \frac{\partial \mathrm{S}^{k1}}{\partial \mathrm{E}_{1l}} = \begin{bmatrix} \dfrac{\partial \mathrm{S}^{k1}}{\partial \mathrm{E}_{11}} \\ \dfrac{\partial \mathrm{S}^{k1}}{\partial \mathrm{E}_{12}} \\ \dfrac{\partial \mathrm{S}^{k1}}{\partial \mathrm{E}_{13}} \end{bmatrix} = \begin{bmatrix} \mathbb{C}^{1l}_{up} \\ \mathbb{C}^{2l}_{up} \\ \mathbb{C}^{3l}_{up} \end{bmatrix}. \tag{61}$$

Moreover, $\mathbf{A}$ and $\mathbf{B}$ are the derivatives of the admissible, finite strain vector, $\mathbf{E}_m$ (see Eqs. (13) and (14)), with respect to the beam deformation measures, defined as follows

$$\mathbf{A} = \frac{\partial \mathrm{E}_{1l}}{\partial \boldsymbol{\Gamma}_N} = \frac{1}{C}\mathbf{I} + \frac{1}{C^2}\boldsymbol{E}_1{\boldsymbol{\Gamma}_N}^{\mathsf{T}} + \frac{1}{C^2}(\boldsymbol{E}_1{\boldsymbol{K}_M}^{\mathsf{T}})(\widetilde{\boldsymbol{\xi}}), \tag{62}$$

$$\mathbf{B} = \frac{\partial \mathrm{E}_{1l}}{\partial \boldsymbol{K}_M} = \frac{1}{C}(\widetilde{\boldsymbol{\xi}})^{\mathsf{T}} + \frac{1}{C}(\boldsymbol{E}_1{\boldsymbol{\Gamma}_N}^{\mathsf{T}})(\widetilde{\boldsymbol{\xi}})^{\mathsf{T}} - \frac{1}{C}(\boldsymbol{E}_1{\boldsymbol{K}_M}^{\mathsf{T}})(\widetilde{\boldsymbol{\xi}})^2, \tag{63}$$

where we have defined $\boldsymbol{\xi} = [0 \quad s_2 \quad s_3]^{\mathsf{T}}$ as the vector of the in-plane cross-section coordinates.

In the above expression of the integral quantities, the linearization requires the calculation of directional derivatives of all the quantities related to the beam configuration manifold. For more details on directional derivatives and linearization procedures for geometrically exact beams, the reader is referred to [61,62,93]. In the following, we report only the new linearization formulas needed in the present work.

Directional derivative of $\bar{\mathbf{R}}$

$$\frac{d}{d\varepsilon}(\bar{\mathbf{R}})_{\varepsilon=0} = \frac{d}{d\varepsilon}(\mathbf{R}\mathbf{R}_0^{\mathsf{T}})_{\varepsilon=0} = \delta\widetilde{\boldsymbol{\vartheta}}\mathbf{R}\mathbf{R}_0^{\mathsf{T}}. \tag{64}$$

Directional derivative of S^{k1}

The second Piola-Kirchhoff stress tensor $\mathbf{S}$ is work-conjugated with the Green-Lagrange strain tensor $\mathbf{E}$, which is in turn expressed as a function of the beam deformation measures, $\boldsymbol{\Gamma}_N$ and $\boldsymbol{K}_M$ (see Eq. (13)). We can compute the directional derivative of the components of the second Piola-Kirchhoff stress tensor, S^{k1}, using the following chain rule

$$\frac{d}{d\varepsilon}(\mathrm{S}^{k1})_{\varepsilon=0} = \left(\frac{\partial \mathrm{S}^{k1}}{\partial \mathrm{E}_{1l_\varepsilon}}\frac{\partial \mathrm{E}_{1l_\varepsilon}}{\partial \varepsilon}\right)_{\varepsilon=0} = \left[\frac{\partial \mathrm{S}^{k1}}{\partial \mathrm{E}_{1l}}\left(\frac{\partial \mathrm{E}_{1l}}{\partial \boldsymbol{\Gamma}_N}\frac{d\boldsymbol{\Gamma}_{N\varepsilon}}{d\varepsilon} + \frac{\partial \mathrm{E}_{1l}}{\partial \boldsymbol{K}_M}\frac{d\boldsymbol{K}_{M\varepsilon}}{d\varepsilon}\right)\right]_{\varepsilon=0} \\ = \mathbb{C}^{kl}_{up}\mathbf{A}C\mathbf{R}^{\mathsf{T}}\delta\boldsymbol{\eta},_s + \mathbb{C}^{kl}_{up}\mathbf{A}C\mathbf{R}^{\mathsf{T}}\hat{\widetilde{\boldsymbol{c}}},_s\delta\boldsymbol{\vartheta} + \mathbb{C}^{kl}_{up}\mathbf{B}C\mathbf{R}^{\mathsf{T}}\delta\boldsymbol{\vartheta},_s\,. \tag{65}$$

For the directional derivatives of $\boldsymbol{\Gamma}_N$ and $\boldsymbol{K}_M$ we refer to, e.g., [61]. **A** and **B** are defined in Eqs. (62) and (63), while $\mathbb{C}_{up}^{kl}$ is given in Eq. (61).

References

[1] F. Auricchio, M. Conti, M. De Beule, G. De Santis, B. Verhegghe, Carotid artery stenting simulation: from patient-specific images to finite element analysis, Med. Eng. Phys. 33 (3) (2011) 281–289.
[2] T. van Manen, S. Janbaz, K.M.B. Jansen, A.A. Zadpoor, 4D Printing of reconfigurable metamaterials and devices, Commun. Mater. 2 (1) (2021) 56.
[3] R.J. Morrison, S.J. Hollister, M.F. Niedner, M.G. Mahani, A.H. Park, D.K. Mehta, R.G. Ohye, G.E. Green, Mitigation of tracheobronchomalacia with 3D-printed personalized medical devices in pediatric patients, Sci. Transl. Med. 7 (285) (2015) 285ra64.
[4] B. Ziaie, X. Velay, W. Saleem, Exploring the optimal mechanical properties of triply periodic minimal surface structures for biomedical applications: a numerical analysis, J. Mech. Behav. Biomed. Mater. 160 (2024) 106757.
[5] J.C. Simo, A finite strain beam formulation. the three-dimensional dynamic problem. part i, Comput. Methods Appl. Mech. Eng. 49 (1) (1985) 55–70.
[6] J.C. Simo, L. Vu-Quoc, A three-dimensional finite-strain rod model. part II: computational aspects, Comput. Methods Appl. Mech. Eng. 58 (1) (1986) 79–116.
[7] J.C. Simo, L. Vu-Quoc, On the dynamics in space of rods undergoing large motions – a geometrically exact approach, Comput. Methods Appl. Mech. Eng. 66 (2) (1988) 125–161.
[8] A. Cardona, M. Geradin, A beam finite element non-linear theory with finite rotations, Int. J. Numer. Methods Eng. 26 (September 1987) (1988) 2403–2438.
[9] E.N. Dvorkin, E. Onte, J. Oliver, On a non-linear formulation for curved timoshenko beam elements considering large displacement/rotation increments, Int. J. Numer. Methods Eng. 26 (7) (1988) 1597–1613.
[10] M.A. Crisfield, A consistent co-rotational formulation for non-linear, three-dimensional, beam-elements, Comput. Methods Appl. Mech. Eng. 81 (2) (1990) 131–150.
[11] A. Ibrahimbegovic, On finite element implementation of geometrically nonlinear Reissner's beam theory: three-dimensional curved beam elements, Comput. Methods Appl. Mech. Eng. 122 (1–2) (1995) 11–26.
[12] A. Ibrahimbegović, F. Frey, I. Kožar, Computational aspects of vector-like parametrization of three-dimensional finite rotations, Int. J. Numer. Methods Eng. 38 (21) (1995) 3653–3673.
[13] A. Ibrahimbegovic, On the choice of finite rotation parameters, Comput. Methods Appl. Mech. Eng. 149 (3) (1997) 49–71.
[14] G. Jelenić, M.A. Crisfield, Geometrically exact 3D beam theory: implementation of a strain-invariant finite element for statics and dynamics, Comput. Methods Appl. Mech. Eng. 171 (1–2) (1999) 141–171.
[15] I. Romero, F. Armero, An objective finite element approximation of the kinematics of geometrically exact rods and its use in the formulation of an energy-momentum conserving scheme in dynamics, Int. J. Numer. Methods Eng. 54 (12) (2002) 1683–1716.
[16] I. Romero, The interpolation of rotations and its application to finite element models of geometrically exact rods, Comput. Mech. 34 (2) (2004) 121–133.
[17] M. Ritto-Correa, D. Camotim, On the differentiation of the rodrigues formula and its significance for the vector-like parameterization of reissner-Simo beam theory, Int. J. Numer. Methods Eng. 55 (9) (2002) 1005–1032.
[18] P. Betsch, P. Steinmann, Frame-indifferent beam finite elements based upon the geometrically exact beam theory, Int. J. Numer. Methods Eng. 54 (12) (2002) 1775–1788.
[19] C. Meier, M.J. Grill, W.A. Wall, A. Popp, Geometrically exact beam elements and smooth contact schemes for the modeling of fiber-based materials and structures, Int. J. Solids Struct. 154 (2018) 124–146.
[20] D. Magisano, L. Leonetti, A. Madeo, G. Garcea, et al., A large rotation finite element analysis of 3D beams by incremental rotation vector and exact strain measure with all the desirable features, Comput. Methods Appl. Mech. Eng. 361 (2020) 112811.
[21] L. Greco, A. Cammarata, D. Castello, M. Cuomo, An objective FE-formulation for cosserat rods based on the spherical bézier interpolation, Comput. Methods Appl. Mech. Eng. 425 (2024) 116947.
[22] L. Greco, D. Castello, A. Cammarata, M. Cuomo, et al., Spherical B-spline interpolation with application to a mixed isogeometric cosserat rod formulation, Comput. Methods Appl. Mech. Eng. 446 (2025) 118239.
[23] C. Meier, A. Popp, W.A. Wall, An objective 3D large deformation finite element formulation for geometrically exact curved kirchhoff rods, Comput. Methods Appl. Mech. Eng. 278 (2014) 445–478.
[24] D. Magisano, L. Leonetti, G. Garcea, Isogeometric analysis of 3D beams for arbitrarily large rotations: locking-free and path-independent solution without displacement DOFs inside the patch, Comput. Methods Appl. Mech. Eng. 373 (2021) 113437.
[25] D. Vo, P. Nanakorn, T.Q. Bui, Geometrically nonlinear multi-patch isogeometric analysis of spatial euler-bernoulli beam structures, Comput. Methods Appl. Mech. Eng. 380 (2021) 113808.
[26] L. Greco, M. Cuomo, D. Castello, A. Scrofani, et al., An updated lagrangian bézier finite element formulation for the analysis of slender beams, Math. Mech. Solids 27 (10) (2022) 2110–2138.
[27] A. Borković, B. Marussig, G. Radenković, Geometrically exact static isogeometric analysis of an arbitrarily curved spatial bernoulli-euler beam, Comput. Methods Appl. Mech. Eng. 390 (2022) 114447.
[28] L. Greco, D. Castello, M. Cuomo, An objective and accurate G1-conforming mixed bézier FE-formulation for kirchhoff-love rods, Math. Mech. Solids 29 (4) (2024) 645–685.
[29] M.S. Park, B.C. Lee, Geometrically non-linear and elastoplastic three-dimensional shear flexible beam element of von-Mises-type hardening material, Int. J. Numer. Methods Eng. 39 (3) (1996) 383–408.
[30] F. Gruttmann, R. Sauer, W. Wagner, Theory and numerics of three-dimensional beams with elastoplastic material behaviour, Int. J. Numer. Methods Eng. 48 (12) (2000) 1675–1702.
[31] S. Pajunen, Large deflection elasto-plastic analysis of beams using kinematically exact elements, Commun. Numer. Methods Eng. 16 (7) (2000) 497–504.
[32] F. Fahrendorf, S. Morganti, A. Reali, T.J.R. Hughes, L. De Lorenzis, Mixed stress-displacement isogeometric collocation for nearly incompressible elasticity and elastoplasticity, Comput. Methods Appl. Mech. Eng. 369 (2020) 113112.
[33] A. Kumar, P. Steinmann, A finite element formulation for a direct approach to elastoplasticity in special cosserat rods, Int. J. Numer. Methods Eng. 122 (5) (2021) 1262–1282.
[34] O. Weeger, D. Schillinger, R. Müller, Mixed isogeometric collocation for geometrically exact 3D beams with elasto-visco-plastic material behavior and softening effects, Comput. Methods Appl. Mech. Eng. 399 (2022) 115456.
[35] D. Magisano, A. Corrado, New robust and efficient global iterations for large deformation finite element analysis of beams and shells with material nonlinearity, Comput. Methods Appl. Mech. Eng. 406 (2023) 115900.
[36] Y. Zhang, Q. Tian, L. Chen, J. Yang, Simulation of a viscoelastic flexible multibody system using absolute nodal coordinate and fractional derivative methods, Multibody Syst. Dyn. 21 (2009) 281–303.
[37] H. Lang, J. Linn, M. Arnold, Multi-body dynamics simulation of geometrically exact cosserat rods, Multibody Syst. Dyn. 25 (3) (2011) 285–312.
[38] A.-N.A. Mohamed, A.A. Shabana, A nonlinear visco-elastic constitutive model for large rotation finite element formulations, Multibody Syst. Dyn. 26 (2011) 57–79.
[39] B. Audoly, N. Clauvelin, P.-T. Brun, M. Bergou, E. Grinspun, M. Wardetzky, A discrete geometric approach for simulating the dynamics of thin viscous threads, J. Comput. Phys. 253 (2013) 18–49.
[40] J. Linn, H. Lang, A. Tuganov, Geometrically exact cosserat rods with kelvin–Voigt type viscous damping, Mech. Sci. 4 (1) (2013) 79–96.
[41] O.A. Bauchau, N. Nemani, Modeling viscoelastic behavior in flexible multibody systems, Multibody Syst. Dyn. 51 (2021) 159–194.

[42] G.G. Giusteri, E. Miglio, N. Parolini, M. Penati, R. Zambetti, Simulation of viscoelastic cosserat rods based on the geometrically exact dynamics of special euclidean strands, Int. J. Numer. Methods Eng. 123 (2) (2022) 396–410.
[43] G. Ferri, D. Ignesti, E. Marino, An efficient displacement-based isogeometric formulation for geometrically exact viscoelastic beams, Comput. Methods Appl. Mech. Eng. 417 (2023) 116413.
[44] G. Ferri, E. Marino, An isogemetric analysis formulation for the dynamics of geometrically exact viscoelastic beams and beam systems with arbitrarily curved initial geometry, Comput. Methods Appl. Mech. Eng. 431 (2024) 117261.
[45] P. Mata Almonacid, H.A. Barbat Barbat, S.H. Oller Martínez, R.L. Boroschek Krauskopf, Inelastic analysis of geometrically exact rods, Centre Internacional de Mètodes Numèrics en Enginyeria (CIMNE), 2008.
[46] F. Auricchio, P. Carotenuto, A. Reali, On the geometrically exact beam model: a consistent, effective and simple derivation from three-dimensional finite-elasticity, Int. J. Solids Struct. 45 (17) (2008) 4766–4781.
[47] E.R. Dasambiagio, P.M. Pimenta, E.M.B. Campello, A finite strain rod model that incorporates general cross section deformation and its implementation by the finite element method, in: Solid Mechanics in Brazil 2009, ABCM Symposium Series in Solid Mechanics, 2, 2009, pp. 145–168.
[48] M.-J. Choi, R.A. Sauer, S. Klinkel, An isogeometric finite element formulation for geometrically exact timoshenko beams with extensible directors, Comput. Methods Appl. Mech. Eng. 385 (2021) 113993.
[49] M.-J. Choi, S. Klinkel, R.A. Sauer, An isogeometric finite element formulation for frictionless contact of cosserat rods with unconstrained directors, Comput. Mech. 70 (6) (2022) 1107–1144.
[50] Ż. Krzysztof Kamil, N. Firouzi, T. Rabczuk, X. Zhuang, Large deformation of hyperelastic modified timoshenko–Ehrenfest beams under different types of loads, Comput. Methods Appl. Mech. Eng. 416 (2023) 116368.
[51] F.M. Fonseca, P.B. Gonçalves, Nonlinear behavior and instabilities of a hyperelastic von mises truss, Int. J. Non Linear Mech. 142 (2022) 103964.
[52] J. Lotfi, S. Khalili, A.R. Damanpack, Micro-macro analysis of hyperelastic auxetic lattice structures under finite-strain regime, Int. J. Mech. Sci. 274 (2024) 109246.
[53] J. Wackerfuß, F. Gruttmann, A mixed hybrid finite beam element with an interface to arbitrary three-dimensional material models, Comput. Methods Appl. Mech. Eng. 198 (27–29) (2009) 2053–2066.
[54] J. Wackerfuß, F. Gruttmann, A nonlinear hu-washizu variational formulation and related finite-element implementation for spatial beams with arbitrary moderate thick cross-sections, Comput. Methods Appl. Mech. Eng. 200 (17) (2011) 1671–1690.
[55] P. Mata, S. Oller, A. Barbat, Static analysis of beam structures under nonlinear geometric and constitutive behavior, Comput. Methods Appl. Mech. Eng. 196 (45–48) (2007) 4458–4478.
[56] P. Mata, S. Oller, A.H. Barbat, Dynamic analysis of beam structures considering geometric and constitutive nonlinearity, Comput. Methods Appl. Mech. Eng. 197 (6–8) (2008) 857–878.
[57] R. Ortigosa, A.J. Gil, J. Bonet, C. Hesch, A computational framework for polyconvex large strain elasticity for geometrically exact beam theory, Comput. Mech. 57 (2016) 277–303.
[58] M.-J. Choi, R.A. Sauer, S. Klinkel, A selectively reduced degree basis for efficient mixed nonlinear isogeometric beam formulations with extensible directors, Comput. Methods Appl. Mech. Eng. 417 (2023) 116387.
[59] S. Klinkel, S. Govindjee, Using finite strain 3d-material models in beam and shell elements, Eng. Comput. (Swansea) 19 (3) (2002) 254–271.
[60] J. Kiendl, M.-C. Hsu, M.C.H. Wu, A. Reali, Isogeometric kirchhoff–Love shell formulations for general hyperelastic materials, Comput. Methods Appl. Mech. Eng. 291 (2015) 280–303.
[61] E. Marino, Isogeometric collocation for three-dimensional geometrically exact shear-deformable beams, Comput. Methods Appl. Mech. Eng. 307 (2016) 383–410.
[62] E. Marino, Locking-free isogeometric collocation formulation for three-dimensional geometrically exact shear-deformable beams with arbitrary initial curvature, Comput. Methods Appl. Mech. Eng. 324 (2017) 546–572.
[63] E. Marino, J. Kiendl, L. De Lorenzis, Isogeometric collocation for implicit dynamics of three-dimensional beams undergoing finite motions, Comput. Methods Appl. Mech. Eng. 356 (2019) 548–570.
[64] F. Auricchio, L. Beirão Da Veiga, T.J.R. Hughes, A. Reali, G. Sangalli, et al., Isogeometric collocation methods, Math. Models Methods Appl. Sci. 20 (11) (2010) 2075–2107.
[65] F. Auricchio, L. Beirão da Veiga, T.J.R. Hughes, A. Reali, G. Sangalli, et al., Isogeometric collocation for elastostatics and explicit dynamics, Comput. Methods Appl. Mech. Eng. 249–252 (2012) 2–14.
[66] T.J.R. Hughes, J.A. Cottrell, Y. Bazilevs, Isogeometric analysis: CAD, finite elements, NURBS, exact geometry and mesh refinement, Comput. Methods Appl. Mech. Eng. 194 (39–41) (2005) 4135–4195.
[67] J.A. Cottrell, T.J.R. Hughes, Y. Bazilevs, Isogeometric analysis: toward integration of CAD and FEA, JohnWiley & Sons, Ltd Registered, 2009.
[68] D. Schillinger, J. Evans, A. Reali, M. Scott, T.J.R. Hughes, et al., Isogeometric collocation: cost comparison with galerkin methods and extension to adaptive hierarchical NURBS discretizations, Comput. Methods Appl. Mech. Eng. 267 (2013) 170–232.
[69] H. Gomez, A. Reali, G. Sangalli, Accurate, efficient, and (iso)geometrically flexible collocation methods for phase-field models, J. Comput. Phys. 262 (2014) 153–171.
[70] L. De Lorenzis, J.A. Evans, T.J.R. Hughes, A. Reali, et al., Isogeometric collocation: neumann boundary conditions and contact, Comput. Methods Appl. Mech. Eng. 284 (2015) 21–54.
[71] R. Kruse, N. Nguyen-Thanh, L. De Lorenzis, T.J.R. Hughes, et al., Isogeometric collocation for large deformation elasticity and frictional contact problems, Comput. Methods Appl. Mech. Eng. 296 (2015) 73–112.
[72] H. Gomez, L. De Lorenzis, The variational collocation method, Comput. Methods Appl. Mech. Eng. 309 (2016) 152–181.
[73] L. Beirão da Veiga, C. Lovadina, a. Reali, Avoiding shear locking for the timoshenko beam problem via isogeometric collocation methods, Comput. Methods Appl. Mech. Eng. 241–244 (2012) 38–51.
[74] F. Auricchio, L. Beirão da Veiga, J. Kiendl, C. Lovadina, a. Reali, et al., Locking-free isogeometric collocation methods for spatial timoshenko rods, Comput. Methods Appl. Mech. Eng. 263 (2013) 113–126.
[75] J. Kiendl, F. Auricchio, T.J.R. Hughes, A. Reali, et al., Single-variable formulations and isogeometric discretizations for shear deformable beams, Comput. Methods Appl. Mech. Eng. 284 (2015) 988–1004.
[76] J. Kiendl, F. Auricchio, A. Reali, A displacement-free formulation for the timoshenko beam problem and a corresponding isogeometric collocation approach, Meccanica (2017) 1–11.
[77] G. Balduzzi, S. Morganti, F. Auricchio, Non-prismatic timoshenko-like beam model: numerical solution via isogeometric collocation, Comput. Math. Appl. 74 (7) (2017) 1531–1541.
[78] A. Reali, H. Gomez, An isogeometric collocation approach for bernoulli-Euler beams and kirchhoff plates, Comput. Methods Appl. Mech. Eng. 284 (2015) 623–636.
[79] J. Kiendl, F. Auricchio, L. Beirão da Veiga, C. Lovadina, A. Reali, et al., Isogeometric collocation methods for the reissner-Mindlin plate problem, Comput. Methods Appl. Mech. Eng. 284 (2015) 489–507.
[80] J. Kiendl, E. Marino, L. De Lorenzis, Isogeometric collocation for the reissner-Mindlin shell problem, Comput. Methods Appl. Mech. Eng. 325 (2017) 645–665.
[81] F. Maurin, F. Greco, L. Coox, D. Vandepitte, W. Desmet, et al., Isogeometric collocation for kirchhoff-Love plates and shells, Comput. Methods Appl. Mech. Eng. 329 (2018) 396–420.
[82] F. Maurin, F. Greco, S. Dedoncker, W. Desmet, et al., Isogeometric analysis for nonlinear planar kirchhoff rods: weighted residual formulation and collocation of the strong form, Comput. Methods Appl. Mech. Eng. (2018).
[83] J.A. Evans, R.R. Hiemstra, T.J.R. Hughes, A. Reali, et al., Explicit higher-order accurate isogeometric collocation methods for structural dynamics, Comput. Methods Appl. Mech. Eng. 338 (2018) 208–240.

[84] M. Torre, S. Morganti, F.S. Pasqualini, A. Düster, A. Reali, Immersed isogeometric analysis based on a hybrid collocation/finite cell method, Comput. Methods Appl. Mech. Eng. 405 (2023) 115856.
[85] D. Ignesti, G. Ferri, F. Auricchio, A. Reali, E. Marino, et al., An improved isogeometric collocation formulation for spatial multi-patch shear-deformable beams with arbitrary initial curvature, Comput. Methods Appl. Mech. Eng. 403 (2023) 115722.
[86] O. Weeger, S.-K. Yeung, M.L. Dunn, Isogeometric collocation methods for cosserat rods and rod structures, Comput. Methods Appl. Mech. Eng. 316 (2017) 100–122.
[87] E. Marino, J. Kiendl, L. De Lorenzis, Explicit isogeometric collocation for the dynamics of three-dimensional beams undergoing finite motions, Comput. Methods Appl. Mech. Eng. 343 (2019) 530–549.
[88] R. Kruse, N. Nguyen-Thanh, L. De Lorenzis, T.J.R. Hughes, Isogeometric collocation for large deformation elasticity and frictional contact problems, Comput. Methods Appl. Mech. Eng. 296 (2015) 73–112.
[89] K.B. Sautter, M. Meßmer, T. Teschemacher, K.-U. Bletzinger, Limitations of the st. venant-kirchhoff material model in large strain regimes, Int. J. Non. Linear Mech. 147 (2022) 104207.
[90] C. Borri, M. Betti, E. Marino, Lectures on solid mechanics, Firenze University Press, 2008.
[91] L. Piegl, W. Tiller, The NURBS Book, Springer, 1997.
[92] E. Marino, S.F. Hosseini, A. Hashemian, A. Reali, Effects of parameterization and knot placement techniques on primal and mixed isogeometric collocation formulations of spatial shear-deformable beams with varying curvature and torsion, Comput. Math. Appl. 80 (11) (2020) 2563–2585.
[93] T.J.R. Hughes, K.S. Pister, Consistent linearization in mechanics of solids and structures, Comput. Struct. 8 (3-4) (1978) 391–397.